RSC Advances

PAPER

View Article Online
View Journal | View Issue



Cite this: *RSC Adv.*, 2025, **15**, 31767

# Solar-driven photocatalytic removal of cefuroxime from water: process optimization *via* machine learning and nature-inspired algorithms

Sara Zeghbib,[a] Noureddine Nasrallah,[a] Haroun Hafsa,[a] Mohammed Kebir,[b] Hichem Tahraoui,[c] Sabrina Lekmine,[e] Walid Zeghbib,[a] Abdeltif Amrane,[d] Fekri Abdulraqeb Ahmed Ali,[f] Farid Fadhillah[f] and Amine Aymen Assadi *[f]

The extensive presence of antibiotics in aquatic environments has raised significant concerns regarding their ecological impact and the potential development of antibiotic-resistant bacteria. This study investigates the photocatalytic degradation of Cefuroxime (CFX) using silver-doped zinc oxide (Ag-ZnO) nanoparticles under solar irradiation. Ag-ZnO nanoparticles were synthesized with varying Ag doping percentages (1, 2, 2.5, and 3 wt%) *via* a sol–gel method, followed by structural and optical characterizations using XRD, SEM-EDS, ATR-FTIR, and UV-Vis spectroscopy. Photocatalytic experiments have revealed that 2 wt% Ag-ZnO exhibited the highest degradation efficiency, attributed to reduced electron–hole recombination and enhanced light absorption in the visible spectrum. The characterization results provided valuable information on the morphological, structural, and compositional features of the prepared catalysts, emphasizing the influence of different silver loadings on their properties. The optical study revealed a decrease in the band gap value from 3.15 eV (ZnO) to 3.01 eV (Ag:ZnO, 2%). Furthermore, the photodegradation kinetics were analyzed, and scavenger tests were performed to examine the role of reactive species, providing a comprehensive understanding of the photocatalytic mechanism. According to the kinetic study, CFX degradation followed pseudo-first-order kinetics, and Hydroxyl radicals (•OH) were identified as the dominant reactive species driving the photodegradation process. To optimize the degradation process, a Decision Tree coupled with the Least Squares Boosting (DT_LSBOOST) algorithm was employed to model and predict CFX photodegradation efficiency based on key operational parameters: reaction time, catalyst dosage, initial CFX concentration, pH, and Ag doping percentage. The optimized DT_LSBOOST model demonstrated high predictive accuracy ($R$ > 0.9996) with minimal root mean square error (RMSE < 0.88). Furthermore, the Dragonfly Algorithm (DA) was implemented to determine the optimal reaction conditions, achieving an experimentally validated degradation rate of 84.25% under optimized conditions (pH = 6.11, catalyst dose = 0.1 g $L^{-1}$, initial CFX = 50 mg $L^{-1}$, 180 min reaction time). The integration of machine learning-based modeling and nature-inspired optimization highlights an effective approach for enhancing photocatalytic processes. The results provide a robust framework for optimizing semiconductor-based water treatment technologies, contributing to sustainable environmental remediation strategies.

Received 22nd June 2025
Accepted 8th August 2025

DOI: 10.1039/d5ra04447b

rsc.li/rsc-advances



## 1. Introduction

In medical practice, antibiotics are extremely important and are used in the treatment of infections because they help in the eradication of dangerous organisms, which consequently improve patient outcomes and public health.[1,2] The extensive utilization and excessive application of antibiotics have led to the unavoidable discharge of their residues into aquatic ecosystems, prompting worries over environmental pollution and the potential emergence of antibiotic-resistant microbes.[3,4]

[a]*Laboratory of Reaction Engineering, Faculty of Mechanical Engineering and Process Engineering, USTHB, BP 32, Algiers, 16111, Algeria*

[b]*Centre de Recherche Scientifique et Technique en Analyses Physico-Chimiques (CRAPC), BP 384, Bou-Ismail, Tipaza 42004, Algeria*

[c]*Laboratory of Biomaterials and Transport Phenomena (LBMPT), University of Médéa, Médéa, Algeria*

[d]*Univ. Rennes – ENSCR/UMR CNRS 6226, 35700 Rennes, France*

[e]*Biotechnology, Water, Environment and Health Laboratory, Abbes Laghrour University, 40004, Algeria*

[f]*College of Engineering, Imam Mohammad Ibn Saud Islamic University (IMSIU), 11432 Riyadh, Saudi Arabia. E-mail: AAAssadi@imamu.edu.sa; Tel: +966 56 326 0210*

Cefuroxime (CFX) belongs to the second-generation cephalosporin family and is a β-lactam antibiotic. Because of its increased stability against β-lactamase enzymes produced by some bacteria, it is frequently used to treat a wide range of bacterial infections, including those that affect the skin, urinary tract, respiratory tract, and other systems.[5,6] Cephalosporin antibiotics, including cefuroxime, have been identified in wastewater at amounts between μg $L^{-1}$ and ng $L^{-1}$. This event prompts environmental apprehensions over its potential effects on aquatic ecosystems and the facilitation of antibiotic resistance.[7,8] The detrimental impact of medication residues, particularly antibiotics, in aquatic ecosystems has emerged as a major concern. Consequently, their efficient removal and treatment have become significant and thoroughly examined study area, with the objective of alleviating environmental hazards and diminishing the emergence of antibiotic resistance.[9,10]

Various methods have been developed to treat antibiotic residues in water before their final discharge into the environment,[10–12] adoption,[13] such as advanced oxidation processes (AOPs),[14–18] biological methods,[19–21] sonocatalyst processes,[22–24] coagulation.[25–27] Research has shown that a wide variety of antibiotics may be eliminated and decomposed by the AOPs into safe and eco-friendly compounds.[28,29] The photocatalysis technique is based on the activation of a semiconductor by light.[30–32]

The absorption of light radiation induces an excitation of electrons on the photocatalyst, which pass from the (BV) valence band to the (BC) conductance band, creating ($e^-/h^+$) electron–hole pairs capable of reacting with oxygen from the air and/or atmospheric humidity to form radicals and initiate oxidation–reduction reactions.[33,34]

Metal oxide semiconductor photocatalysts are a promising approach for applying environmental remediation due to their high stability, controlled morphologies, physical properties, variable surface chemistry, textural qualities, and distinct crystalline nature.[35]

Zinc oxide (ZnO), a metal oxide semiconductor, has the advantage of being a non-toxic, environmentally friendly compound. It is also thermally and chemically stable, and the raw materials required for its production are abundant. However, the energy of its wide bandgap (∼3.37 eV) presents a major challenge, limiting its effectiveness to wavelengths in the UV range, which account for only 5% of sunlight.[36]

To exploit solar radiation, it is necessary to modify the electronic properties of ZnO nanostructures. It is therefore necessary to find solutions to increase the quantity of photons that can absorb, and make it more efficient in sunlight. Transition metal (TM) doping in the ZnO crystal lattice is one of the best-known strategies for adjusting the bandgap of ZnO to make it an active photocatalyst in visible light and prolonging the time life of electron holes.[37]

Doping ZnO with different metals enhances its effectiveness, as Cu:ZnO NPs,[38] Mn:ZnO NPs,[39] Ce:ZnO NPs[40] and Fe:ZnO NPs,[41] Ni:ZnO NPs.[42] It is important to note that not all transition metals boost efficiency; in fact, some of them actually reduce it due to an increase in electron–hole recombination.[43]

Recent research has demonstrated substantial enhancements in photocatalytic performance across a range of applications, including hydrogen evolution, $CO_2$ reduction, and the degradation of recalcitrant organic pollutants such as pharmaceutical residues and synthetic dyes.[44] Among these, Ag doped ZnO nanomaterials have garnered attention due to their improved light-harvesting and charge separation capabilities. Specifically, ZnO doped with 3 wt% Ag has been reported to degrade tetracycline and amoxicillin with efficiencies of 92.1% and 76.4%, respectively, within 90 minutes of visible light exposure, accompanied by total organic carbon (TOC) removal of 42.7% and 31.3%.[45] Moreover, ZnO doped with 6 wt% Ag, synthesized *via* a mechanochemical combustion route, has shown excellent photocatalytic performance in the degradation of famotidine a model pharmaceutical contaminant achieving up to 88% removal efficiency under visible light within 90 minutes.[46]

As regards this work, the photocatalytic degradation of the antibiotic cefuroxime (CFX) was studied using silver-doped ZnO (Ag:ZnO) nanoparticles under solar irradiation. Ag:ZnO nanoparticles with different Ag concentrations (1, 2, 2.5 and 3 wt%) were synthesized by the sol–gel method, and their characterization was carried out using various analytical techniques (XRD, SEM-EDS, ATR-FTIR and UV-Vis) to evaluate their structural, morphological, and optical properties. The photocatalytic efficiency of these materials was analyzed as a function of several parameters, including pH, initial antibiotic concentration and photocatalyst dose. Advanced modeling was developed by using a decision tree algorithm coupled with least squares boosting (DT_LSBOOST) to predict the CFX degradation rate according to experimental conditions. Subsequently, optimization of the degradation conditions was carried out by using the Dragonfly Algorithm (DA), allowing the identification of optimal experimental parameters. In addition, an application was developed in MATLAB to ensure real-time prediction and optimization of the CFX degradation rate according to operating conditions. This integrated approach, combining modeling, optimization and experimentation, was implemented with the aim of improving the efficiency of photocatalytic processes for the treatment of water contaminated by antibiotics.

This work proposes a novel and original approach combining the synthesis and characterization of optimized Ag-ZnO nanoparticles with advanced modeling based on the DT_LSBOOST algorithm and optimization by the Dragonfly Algorithm (DA) for the photocatalytic degradation of cefuroxime (CFX). Unlike conventional studies that focus solely on experimental optimization, this study integrates advanced artificial intelligence to predict with high accuracy the photodegradation efficiency and identify optimal conditions. In addition, the development of an interactive MATLAB application allows real-time optimization, thus facilitating the adoption of this technology for the treatment of contaminated water. This multidisciplinary integration between advanced materials, machine learning, and computational optimization opens new perspectives for intelligent and efficient photocatalytic systems.

## 2. Materials and methods

### 2.1. Chemicals reagents

The chemical reagents utilized in this investigation were acquired from Sigma Aldrich, And employed without purification: polyvinyl alcohol (PVA, >98%, Sigma-Aldrich Co., USA), silver nitrate ($AgNO_3$, >99%, Sigma-Aldrich Co., USA), and zinc acetate dihydrate ($Zn(CH_3COO)_2$ $2H_2O$, >99%, Sigma-Aldrich Co., USA). Distilled water was used to prepare the solution. However, Pharmaliance, an Algerian pharmaceutical laboratory firm, provided the antibiotic's main active component, which was utilized exactly as supplied without any additional purification.

### 2.2. Preparation of the photocatalyst Ag doped ZnO

ZnO NPs were successfully prepared using a simple method, zinc acetate dihydrate $Zn(CH_3COO)_2 \cdot 2H_2O$ was dissolved in distilled water. The resulting solution was continuously agitated for 2 h on a magnetic stirrer with heating at 100 °C. The obtained powder was first dried in an oven at 100 °C for 24 h and subsequently calcined at 450 °C for three hours in the furnace to produce a nanocrystalline powder of ZnO with enhanced structural properties.

Silver doped ZnO NPs were prepared using a method similar to that described above, with silver incorporated at different percentages of Ag (1, 2, 2.5 and 3 wt%), this approach ensures uniform doping while maintaining the fundamental synthesis process. Zinc solution was prepared by dissolving zinc acetate dehydrate in distilled water. Separately, silver nitrate ($AgNO_3$) was dispersed in distilled water and added to the above-prepared solution, and agitated for 1 h. Additionally, a PVA solution was prepared with a PVA : ZnO ratio of 1 : 5 and subsequently added to the initial solution which was homogenized by stirring for 2 h with a magnetic stirrer under heating at 100 °C. After being dried for 24 hours at 100 °C in the oven, the resulting powder was calcined for three hours at 450 °C in a furnace to obtain a nanocrystalline phase powder.

### 2.3. Materials characterization

The synthesized photocatalysts with different percentages of ZnO-doped silver, were characterized using several physico-chemical methods to understand thier morphology and structure. X-ray diffraction (XRD) was conducted using Bruker D8 Advance, PANalytical Co. Ltd, Netherlands) equipped with a Cu Kα anticathode ($\lambda = 1.54056$ Å). The recording speed of 0.01° $s^{-1}$ in the range (5°–80°) allows the identification and analysis of the crystallite phase present in the prepared materials, thanks to HIghschor plus software. A scanning electron microscope (SEM; Quanta 650) coupled with an energy-dispersive X-ray spectroscopy (EDX) device was used to analyze the microstructure and elemental composition of the samples. The principal functional groups were identified by ATR-FTIR spectroscopy using a Bruker Alpha One in the region (400–4000 $cm^{-1}$). The UV-visible spectrophotometer used for optical characterization was a Specord 210 (Analytical Jena, Germany) equipped with an integrating sphere. Polytetrafluoroethylene (PTFE) was employed as the conventional standard, and measurements were recorded over the wavelength range of 190–1100 nm.

### 2.4. Photocatalytic experiment conditions

In ordre to evaluate the photocatalytic activity of the pure ZnO and Ag:ZnO NPs, an aquouse solution of CFX was used. The photocatalytic process was performed in batch mode. Optimization experiments were conducted to identify the ideal degradation conditions by varying parameters such as pH, initial concentration, and catalyst amount. The solutions were initially stirred in the dark for 30 minutes to establish the adsorption–desorption equilibrium, followed by exposure to sunlight for three hours. The absorbances of CFX were determined every 30 minutes by using a UV-visible spectrophotometer (Shimadzu, Model UV-1800) at the maximal absorption wavelength of CFX, $\lambda_{max} = 281$ nm. The photodegradation efficiency for each experiment was calculated using the following formula;

$$\text{Photodegradation efficiency} = \frac{C_0 - C(t)}{C_0} \times 100 \quad (1)$$

where $C_0$ represents the initial concentration of CFX after adsorption, and $C(t)$ denotes the concentration after irradiation at time ($t$).

### 2.5. Measuring total organic carbon (TOC)

The mineralization efficiency of CFX during photocatalytic degradation over Ag:ZnO was evaluated by measuring the Total Organic Carbon (TOC) using the Sievers TOC-M9 analyzer. Based on the TOC values from eqn (2), the residual mineralization [%] of the CFX reaction solutions was calculated under ideal experimental circumstances.

$$\text{The residual mineralization } (\%) = \left(1 - \frac{\text{COT}}{\text{COT}_o}\right) \times 100 \quad (2)$$

where $TOC_o$ and TOC stand for the starting concentration and the concentration after time $t$, respectively.

### 2.6. Decision tree coupled with the least squares method

DT is a supervised learning algorithm widely used in classification and regression.[47,48] It works by segmenting the feature space into homogeneous subgroups *via* a tree structure, where each node represents a decision based on a specific feature. Its ease of interpretation and ability to model nonlinear relationships make it a powerful tool.[47,48] However, it has several drawbacks: it is prone to overfitting, particularly when the tree is deep, and it is sensitive to data variations, which can lead to high variance and instability in predictions.[47,48]

LSBOOST is a variant of boosting that optimizes a set of weak models by minimizing the mean squared error. It sequentially builds decision trees, where each new tree corrects the errors of the previous one by reducing the gap between predictions and actual values. LSBOOST is particularly effective at improving model accuracy while limiting overfitting.[47,48] Coupling DT with LSBOOST (DT_LSBOOST) overcomes the limitations of DT while exploiting its strengths. By combining multiple weak trees instead of a single complex tree, LSBOOST reduces variance and

improves model stability.[47,48] This approach also allows for better generalization to new data, minimizing overfitting while maintaining high expressiveness. In addition, iterative error correction significantly improves prediction accuracy, making this coupling particularly effective for handling complex and nonlinear relationships between variables.[47,48]

In this study, the prediction of the photodegradation rate of CFX in the presence of Ag-ZnO material was performed using the DT_LSBOOST algorithm. The database was created by integrating the parameters optimized in this research and considering different experimental conditions. The input variables used include reaction duration (X1), the amount of catalyst applied (X2), the initial CFX concentration (X3), the pH of the medium (X4), and the silver doping percentage (X5).

To ensure better model convergence, the data set was normalized to the interval [−1, 1]. This step mitigated the influence of scaling differences between the different variables on model training. Subsequently, the data were divided into three distinct sets: 70% were used for training, 15% for testing, and the remaining 15% for validation, thus ensuring a reliable assessment of the predictive model's performance. Hyperparameter optimization was carefully performed to improve model accuracy. For DT, adjustments were made to several parameters, including the minimum leaf size, the maximum number of splits, the minimum parent node size, and the activation of substitution splits, to maintain an optimal balance between complexity and interpretability.[47,48] For LSBOOST, optimization focused on the number of iterations, the learning rate, and the number of variables selected at each split, with the aim of gradually reducing residual errors.[47,48] The learning rate, set at 0.1, ensured gradual convergence while maintaining model stability. The effectiveness of the final model was assessed using two key metrics: the correlation coefficient ($R$) and the root mean square error (RMSE).[49–52] The $R$ coefficient was used to determine the model's ability to explain the variance in the results obtained, while the RMSE was used to measure the average deviation between predictions and experimental values.[53–57]

# 3. Results and discussions

## 3.1. Catalytic characterization

**3.1.1. ATR-FTIR analysis.** ATR-FTIR spectroscopy is a technique that utilizes the infrared absorption bands of a molecule to identify its chemical groups. The various chemical bonds oscillate at specific frequencies when subjected to infrared light. By examining and interpreting these absorbed frequencies, one can ascertain the functional groups present in pure ZnO and the silver-modified ZnO powders were subjected to ATR-FTIR spectroscopy analysis.

Moreover, ATR-FTIR analyses confirmed the formation of the different crystallographic phases of ZnO prepared by sol–gel method, with significant absorption bands observed in the following wavelentgh (or frequency): 2952, 1643, 1564, 658 $cm^{-1}$ and they correspond to the functional group OH, respectively. The location of the bands at 2952 and 1564 $cm^{-1}$ can be attribueted to the C–H groups of the organic compound (PVA).

In addition, the results confirmed that the modified samples show a peak corresponding to the silver, and thier intensity increases as the concentration of the doping agent increases. Finally, another pic has been detected at 510 $cm^{-1}$, which can be attributed to Zn–O bond vibrations. Attenuated Total Reflectance-Fourier Transform Infrared (ATR-FTIR) spectroscopy is a robust analytical method that utilizes the infrared absorption bands of molecules to ascertain the precise chemical groups present in a sample. Exposure to infrared light causes different chemical bonds inside a molecule to oscillate at specific frequencies. This work has analyzed the chemical structures of both pure ZnO and silver-modified ZnO powders using ATR-FTIR spectroscopy.

The ATR-FTIR results reveale the existence of several crystallographic phases of ZnO perpared through the sol–gel technique. Prominent absorption bands were seen at distinct wavelengths, specifically at 2952, 1643, 1564, and 658 $cm^{-1}$. The bands correspond to distinct functional groups, with the band at 2952 $cm^{-1}$ and the one at 1564 $cm^{-1}$ attributable to the C–H stretching and bending vibrations of the chemical molecule polyvinyl alcohol (PVA) utilized in the production process. The existence of these bands signifies the conservation of organic constituents inside the ZnO matrix, potentially contributing to structural stabilization.

Additionally, the investigation demonstrated that the altered ZnO samples displayed a unique peak associated with silver. The peak's strength notably increased with larger doses of the silver doping agent, indicating effective incorporation of silver into the ZnO matrix. The heightened intensity signifies improved surface contacts and possible synergies between silver and ZnO, advantageous for diverse applications such as catalysis, and sensing.

A peak seen at 510 $cm^{-1}$ was ascribed to the vibrations of Zn–O bonds, hence corroborating the effective synthesis of ZnO. This peak is essential as it offers insight into the bonding properties and structural integrity of the ZnO network underscoring the significance of the sol–gel technique in the production of high-quality ZnO materials. The ATR-FTIR spectroscopy results elucidate the chemical and structural characteristics of both pure and silver-modified ZnO, facilitating its prospective applications in advanced materials research (Fig. 1).

**3.1.2. X-ray diffraction.** XRD analysis was conducted to examine the composition, determine the phase structure, and evaluate the purity of the synthesized oxides. Fig. 2 illustrates the XRD pattern of pure ZnO and Ag:ZnO with different Ag concentrations (1, 2, 2.5 and 3 wt%). Pure ZnO NPs showed a diffraction peaks at $2\theta$ values of 31.94°, 34.59°, 36.43°, 47.69°, 56.75°, 63°, 66.52°, 68.01° and 69.23° associated to the wurtzite hexagonal phase of ZnO (JCPDS card no. 036-1451),[58] that corresponds to diffraction of the (100), (002), (101), (102), (110), (103), (200), (112) and (201) planes, respectively. Also, It was marked that no additional peaks corresponding to impurities were detected, that indicate the high purity of the prepared ZnO phase.

For the observation of XRD patterns of Ag:ZnO NPs showed the presence of two minor diffraction peaks indicated the formation of crystalline silver clusters within the ZnO

 

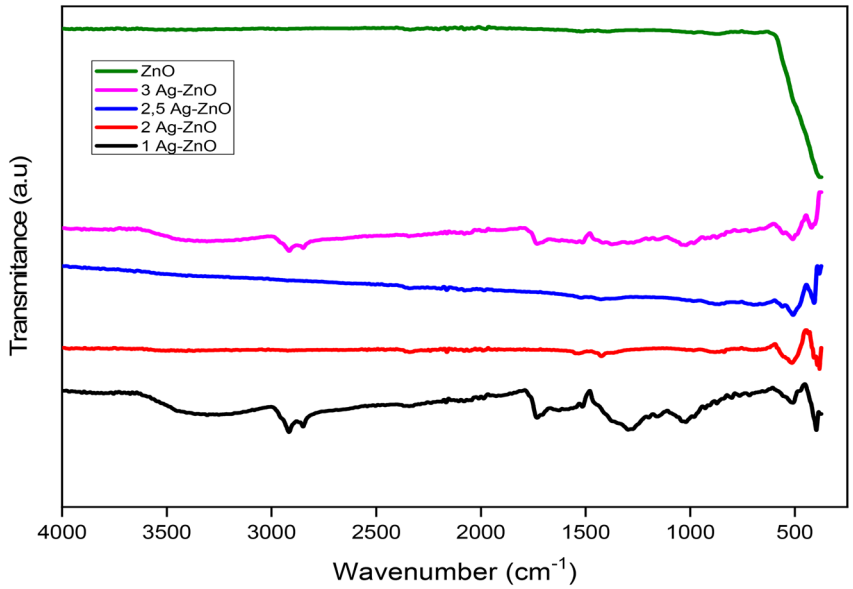


Fig. 1 ATR-FTIR analysis ZnO, Ag:ZnO (1%), Ag:ZnO (2%), Ag:ZnO (2.5%), Ag:ZnO (3%) samples, respectively.

nanoparticles at 38, 29° and 44, 46° which are related to the (fcc) face centered cubic of the element metallic silver (JCPDS card no. 04-0783)[59] and can be assigned as Ag(111) and Ag(200) planes, respectively. This materials modfication could enhance the photocatalytic performances by improving the charge separation and light absorption.

The diffractograms obtained from the Ag:ZnO samples revealed a clear absence of peaks associated with impurity phases, notably those characteristic of silver oxide. This finding is significant as it suggests that the synthesis process effectively prevented the formation of unwanted by-products that could compromise the material's properties. Additionally, comparing the Ag:ZnO composite to pure ZnO the analysis showed no significant shifts in peak positions. This stability in peak positioning indicates the silver particles are predominantly situated on the surface of the ZnO nanoparticles, rather than infiltrating the ZnO lattice structure.[60]

The lack of intermixing between silver and zinc also rules out the possibility of silver ions substituting for zinc sites within the ZnO crystal structure. Such behavior is critical, as it maintains the integrity of the ZnO matrix, ensuring its inherent properties remain intact. This surface localization of silver is advantageous

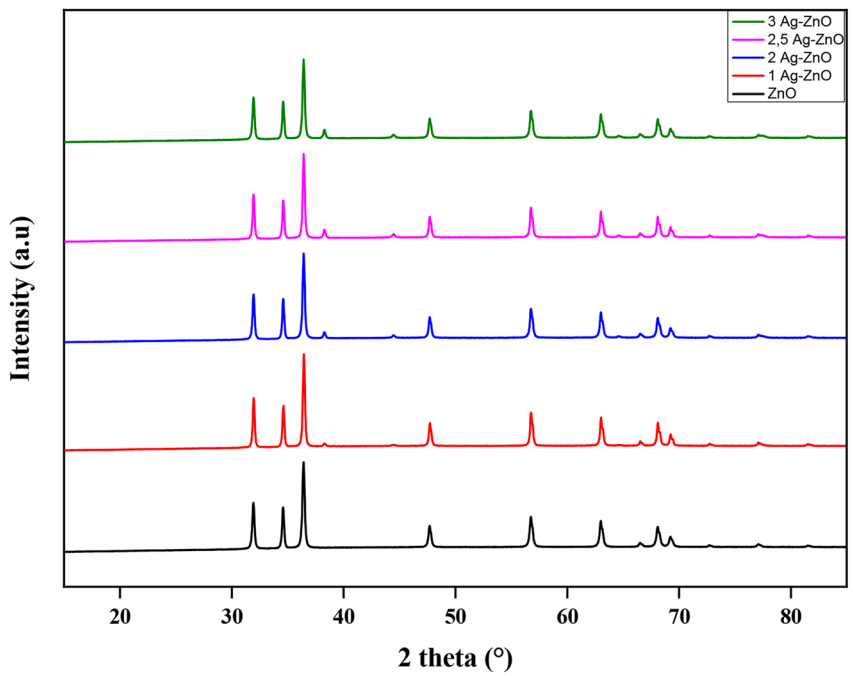


Fig. 2 XRD patterns of ZnO, Ag:ZnO (1%), Ag:ZnO (2%), Ag:ZnO (2.5%), Ag:ZnO (3%) samples.

for applications where surface interactions play a vital role, such as in catalysis and photocatalysis, where surface phenomena can significantly influence the reactivity and efficiency of the materials. Overall, these results give valuable information on the structural characteristics of the Ag:ZnO system and highlight the potential for tailored applications without the complications introduced by impurity phases.

**3.1.3 Scanning electron microscopy (SEM) analysis.** Fig. 3 shows the surface morphology of Ag:ZnO and pure ZnO nanoparticles. The images demonstrate that both nanoparticle forms possess a *quasi*-spherical morphology that indicate a comparable structural property. One explanation for the resemblance is the uneven dispersion of silver dopants on the ZnO nanoparticle surface. Consequently, the nanoparticles exhibit asymmetrical geometries and the aggregation of diminutive crystalline entities. This aggregation may affect the overall characteristics of the materials and emphasizing the intricate interactions between the ZnO matrix and the silver dopants.[61]

**3.1.4. Elementary analysis (EDS).** The chemical purity and elemental composition of Ag:ZnO and pure ZnO NPs were meticulously examined using Energy Dispersive Spectroscopy (EDS), as depicted in Fig. 4. This approach facilitated the precise identification of elemental elements inside the samples. The EDS results verified the existence of zinc (Zn), oxygen (O), and silver (Ag) by identifying their distinctive peaks in the spectrum. This study offers compelling evidence for the effective integration of silver into the ZnO nanoparticles, demonstrating that the doping technique successfully modified the material's composition without adding substantial contaminants.

Furthermore, the elemental analysis disclosed the relative quantities of each element in the samples, which is essential for comprehending how doping with silver affects ZnO's properties. Table 1 presents a detailed description of the EDS data, illustrating the quantitative measures that underscore the efficacy of the doping process and the overall chemical purity of the produced materials. This result not only corroborates the synthesis process but also establishes a foundation for subsequent inquiries into the functional properties of silver-doped ZnO nanoparticles, especially in applications like catalysis and photocatalysis.

**3.1.5. Optical properties.** To investigate the optical characteristics of the nanoparticles and assess the impact of silver doping on the ZnO lattice, UV-visible spectroscopy was used. With the reflectance measurement, we can calculate a function representing the absorption coefficient ($\alpha$) of the samples. This function is called the Kubelka–Munk function (KM):[62]

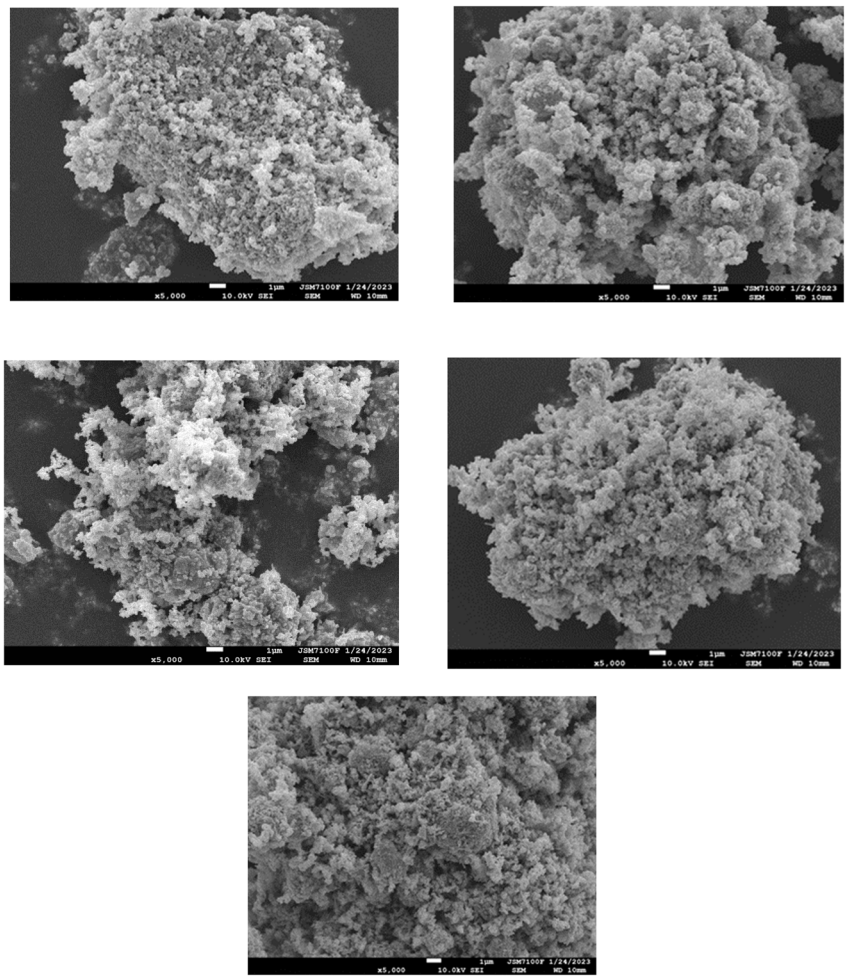

Fig. 3 Scanning electron microscopy images of ZnO, Ag:ZnO (1%), Ag:ZnO (2%), Ag:ZnO (2.5%), Ag:ZnO (3%) samples, respectively.

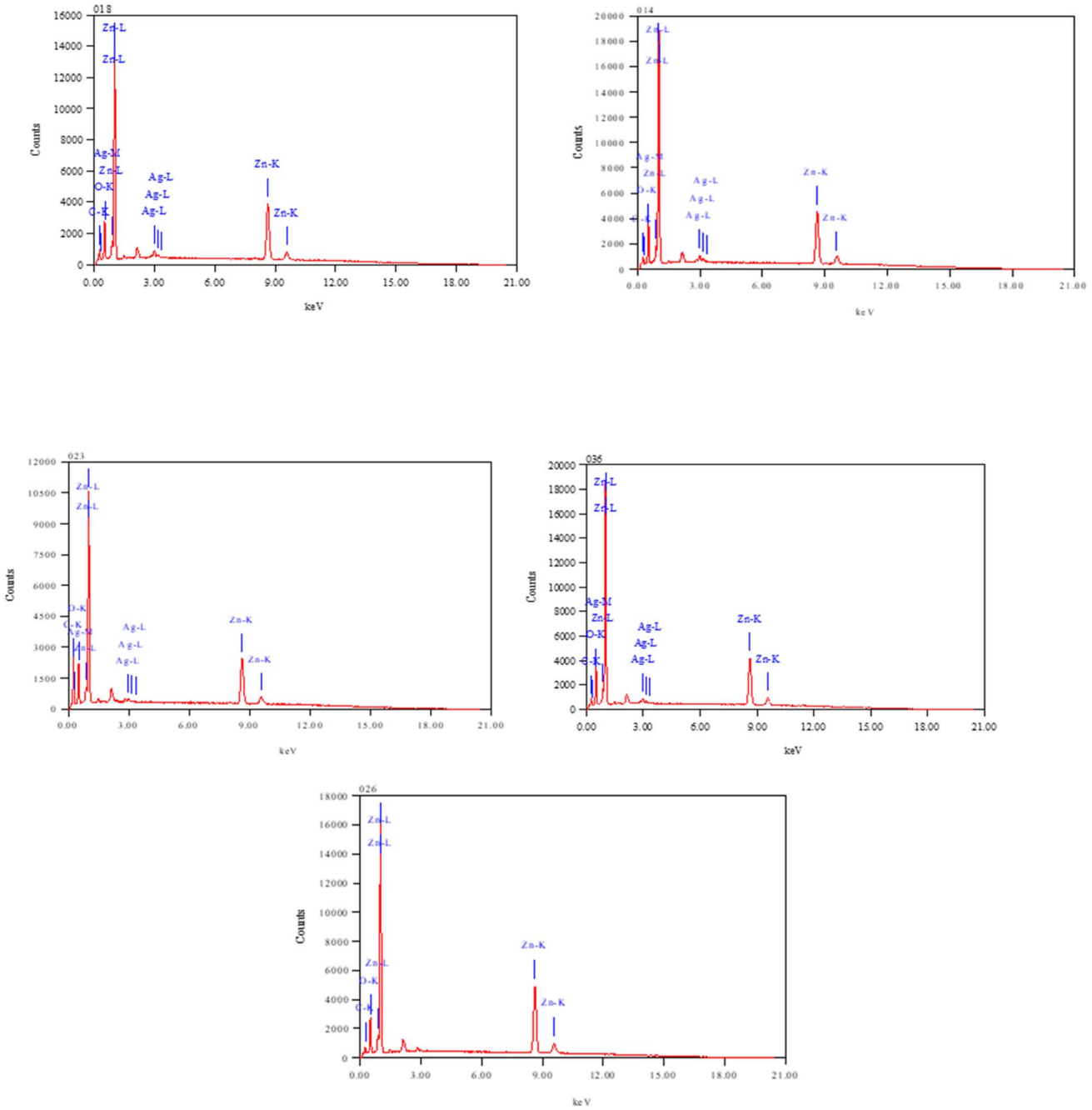


Fig. 4 EDX identification of ZnO, Ag:ZnO (1%), Ag:ZnO (2%), Ag:ZnO (2.5%), Ag:ZnO (3%) samples.

$$\mathrm{KM} = \alpha = \frac{(1-R^2)}{2R} \quad (3)$$

The effective absorption coefficient ($\alpha$) varies with ($E_g$) the optical band gap and with the energy of the absorbed photon ($h\nu$) according to the Tauc equation:[63]

Table 1 Chemical composition of the prepared ZnO, Ag:ZnO (1%), Ag:ZnO (2%), Ag:ZnO (2.5%), Ag:ZnO (3%) samples

| Element | Pure ZnO (wt%) | Ag:ZnO (1%) (wt%) | Ag:ZnO (2%) (wt%) | Ag:ZnO (2.5%) (wt%) | Ag:ZnO (3%) (wt%) |
|---|---|---|---|---|---|
| Zn | 82.37 | 46.99 | 74.12 | 71.81 | 73.67 |
| O | 11.21 | 16.04 | 15.14 | 13.87 | 14.81 |
| C | 6.42 | 36.25 | 8.14 | 11.58 | 8.27 |
| Ag | 0 | 0.72 | 2.6 | 2.74 | 3.35 |

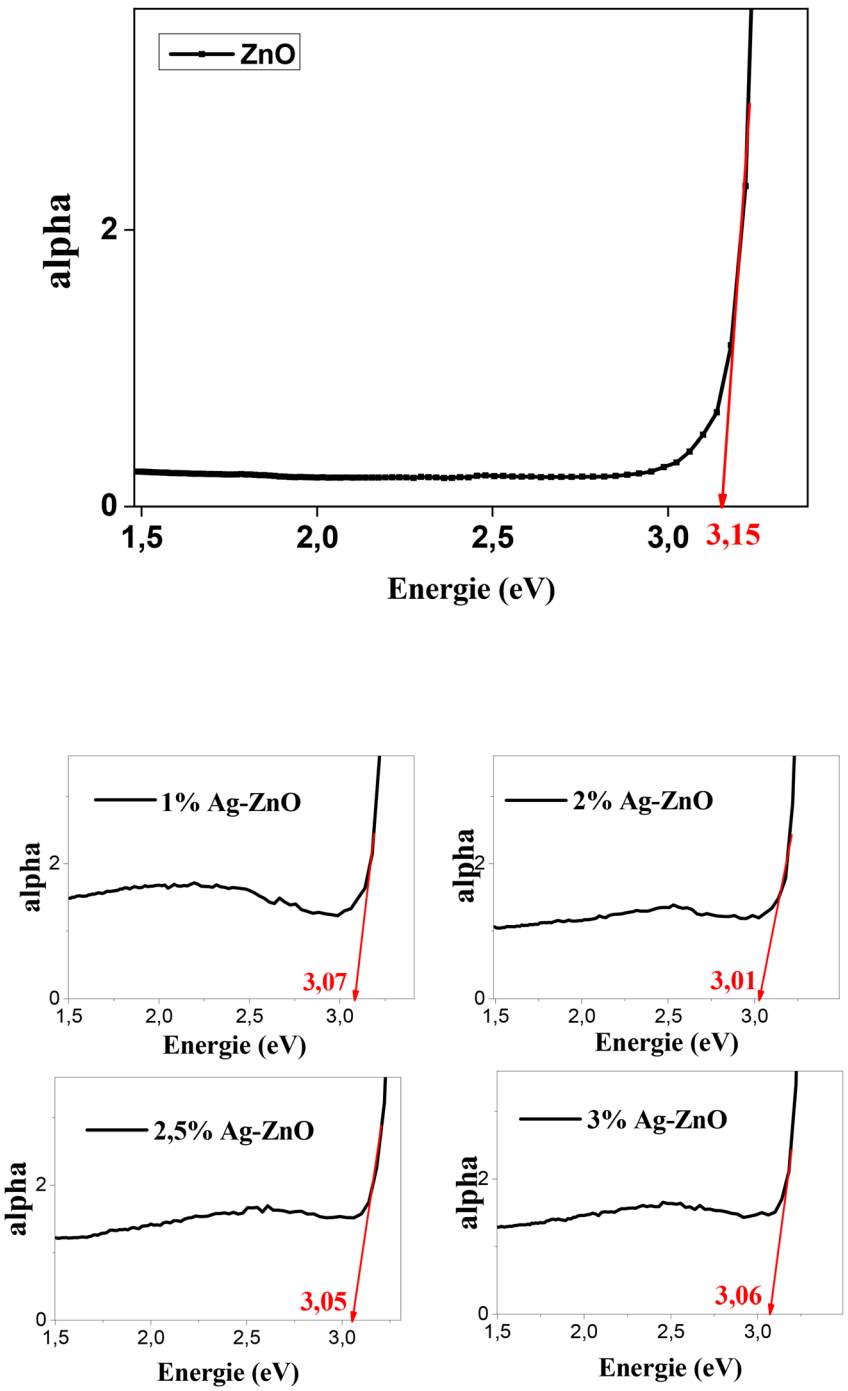


Fig. 5 The $(\alpha h\nu)^2$ *vs.* $(h\nu)$ curves for band gap determination of the pure ZnO and the Ag:ZnO.

$$(\alpha h\nu)^{1/n} = B(h\nu - E_g) \quad (4)$$

where $h$ is Planck's constant, $\nu$ is the frequency, $B$ is a constant and generally called band tailing parameter, and exponent $n$ depends on the transition type. For the direct transition, the value of $n$ is equal to 1/2. The intercept between the $x$-axis $(h\nu)$ and the tangent line at the inflection point gives the experimental band gap of the powder samples.[64]

Band gaps of 3.15 eV, 3.07 eV, 3.01 eV, 3.05 eV, and 3.06 eV were determined for pure ZnO and the 1, 2, and 2.5, 3 wt% Ag:ZnO NPs, respectively as seen in Fig. 5.

It was observed that the modification of ZnO nanoparticles with Ag reduced the optical band gap compared to pure ZnO NPs, This decrease in band gap energy increases the photoactivity of the Ag:ZnO catalyst when exposed to visible light.

### 3.2. Photocatalytic activity and degradation kinetics

The impact of several parameters affecting the photodegradation of cefuroxime in the presence of modified ZnO under sunlight is thoroughly examined in the subsequent experiments. The parameters encompass the concentration of cefuroxime, the dose of the modified ZnO photocatalyst, the pH of the reaction solution, and the duration of sunlight exposure. The effects of alterations to ZnO, including metal or nonmetal doping and the integration of co-catalysts such silver nanoparticles, are examined to assess their contribution to improving photocatalytic efficiency. The interaction of these elements is essential in ascertaining the degradation rate, the efficacy of mineralization, and the overall performance of the photocatalyst under sun irradiation. The research offers significant insights for enhancing reaction conditions and augmenting the practical use of modified ZnO for environmental remediation.

**3.2.1. Effect of doping percentage.** This part of work investigates the impact of various silver doping ratios (1%, 2%, 2.5%, and 3%) on ZnO nanoparticles on the photocatalytic degradation efficiency of cefuroxime (CFX). Experiments were conducted under uniform operating conditions, utilizing a catalyst dosage of 0.1 g $L^{-1}$ in a pH-neutral solution and a constant initail CFX concentration of 10 mg $L^{-1}$. The photocatalytic efficiency of each doping ratio was assessed by observing the degradation rate of CFX under solar irradiation, with the objective of identifying the optimal doping level for rate efficiency.

In contrast to the undoped ZnO nanoparticles, the silver doped ZnO nanoparticles had the best removal effectiveness for CFX after 180 minutes, as seen in Fig. 6 below. The photocatalytic activity of ZnO considerably boosted when the silver concentration was raised to 2 wt%. However, photocatalytic efficiency decreased as the silver concentration went beyond Two weight percent (2 wt%), underscoring the need of figuring out the ideal silver doping ratio. Additionally, the studies have also shown that there is an optimum amount of Ag-doped ZnO, and there are different optimum amounts of Ag depending on the synthesis method and the dispersion of silver within ZnO.[65]

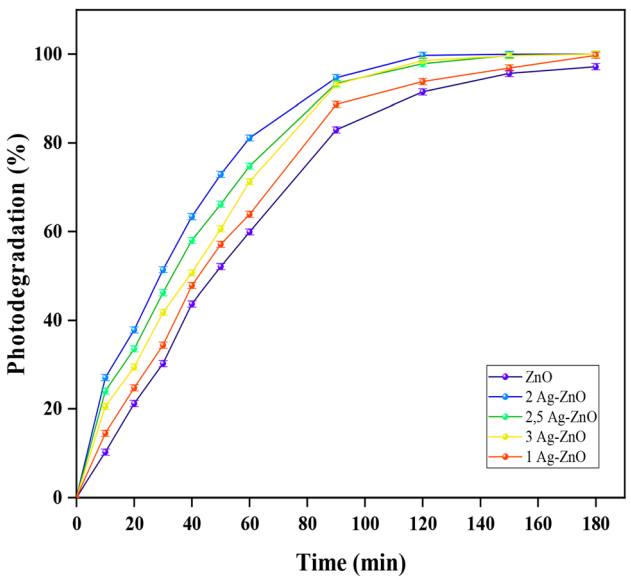


Fig. 6 Effect of doping percentage on percentage degradation of CFX (catalyst dose 0.1 g $L^{-1}$, CFX conc. 10 ppm and free PH).

At moderate Ag concentrations a photocatalytic enhancement is observed due to the significant reduction in electron–hole interaction on the catalyst surface upon exposure to sunlight. When $Ag^{+}$ ions are incorporated into the crystalline structure of ZnO nanoparticles, they modify the electronic structure of the generated species. These silver cations attract the excited electrons from the valence band, effectively preventing their recombination and thereby inhibiting hole–electron recombination within the semiconductor. Consequently, silver and the liberated electrons in the conduction band generate more superoxide on the ZnO surface. At the same time, the holes exhibit strong oxidizing properties, leading to the formation of hydroxyl radicals through reactions with water molecules. The increased production of superoxide and hydroxyl radicals, coupled with the suppression of hole–electron recombination, contributes to improved oxidation–regeneration reactions. As a result, CFX elimination efficiency under solar radiation is improved by the oxidation–regeneration events, guaranteeing more efficient photocatalytic degradation.[37] At high Ag concentrations, secondary phases such as AgO can form, disrupting the crystal structure of ZnO, moreover Too high an Ag concentration can cover the active sites of ZnO, thus reducing the surface area available for adsorption of reactants and decreasing photocatalytic efficiency, which explains the presence of a doping optimum.[51]

Since, the best CFX degradation efficiency (%) was observed with 2 wt% Ag:ZnO, subsequent the other experiments were completed using this dosage ratio of silver doped ZnO compared to higher doping concentrations of 2.5% and 3% Ag-doped ZnO. This enhancement can be attributed to the prolonged lifetime of charge carriers, as the photogenerated electrons are effectively trapped, thereby suppressing electron–hole recombination during irradiation. Metal nanoparticles incorporated into the ZnO matrix, especially those involving heavy or noble metal ions, act as electron sinks, leading to improved photocatalytic performance.[44] The photocatalytic degradation of CFX can be formally described by the Langmuir–Hinshelwood kinetic model:

$$r = -\frac{dC}{dt} = \frac{kKC}{1 + KC} \quad (5)$$

where, $r$: the pollutant degradation rate (mol ($L^{-1}$ $min^{-1}$)), $k$: reaction rate constant (mol ($L^{-1}$ $min^{-1}$)), $K$: adsorption constant of the reactant (L $mol^{-1}$), $C$: pollutant concentration (mol $L^{-1}$).

When the adsorption is relatively weak and the concentration of the reactant is low ($KC \ll 1$), by ignoring $KC$ in the denominator and integrating by time $t$, the above equation can be simplified to the pseudo-first order kinetic model equation:

$$\ln\left(\frac{C_o}{C}\right) = kt \quad (6)$$

Table 2 Photodegradation percentage and kinetic parameters for the photodegradation of CFX on pure ZnO and Ag:ZnO with different (wt%)

| Catalyst type | Ag (wt%) | $k$ (min$^{-1}$) | $R^2$ | $t^{1/2}$ (min) | Photodegradation (%) |
|---|---|---|---|---|---|
| Pure ZnO | — | 0.015 | 0.98 | 46.2 | 97.19 |
| Ag-doped ZnO | 1 | 0.017 | 0.99 | 40.77 | 99.75 |
| | 2 | 0.026 | 0.98 | 26.65 | 99.97 |
| | 2.5 | 0.009 | 0.99 | 77.01 | 99.77 |
| | 3 | 0.016 | 0.98 | 43.32 | 99.63 |

The concentrations of CFX in the aqueous solution at a specific irradiation time are expressed by $C_o$ and $C_t$, where as $k$ represents the apparent rate reactions constant. The rate constant ($k$) and the coefficient of correlation data are shown in Table 2.

The rate constant ($k$) for each experiment was calculated by determining the slope of the plot of the linear relationship of ln $C_o/C$ with irradiation time (Fig. 7).

**3.2.2. Effect of catalyst dose.** The impact of catalyst amount on the rate of CFX photodegradation is illustrated in Fig. 8, experiments were conducted using various Ag-ZnO amounts Rangong from 0.05 to 0.4 g L$^{-1}$, to investigate its influence on the photodegradation efficiency. The results demonstrated a noticeable trend, with the degradation improving as the Ag-ZnO dosage increased up to 0.1 g L$^{-1}$ in a 10 mg L$^{-1}$ CFX solution. However, further increases in the catalyst dosage did not significantly impact the degradation process. This behavior can be partially explained by the increased turbidity of the reaction medium at higher catalyst concentrations, which significantly hinders light penetration through the suspension and consequently reduces the photoactivation volume. Although this effect was not quantitatively evaluated in the present study *via* UV-Vis transmittance or scattering measurements, a marked increase in opacity was consistently observed during the experiments with higher catalyst loadings. This observation is consistent with previous findings in the literature, where excessive photocatalyst concentrations have been shown to scatter or block incident light, thereby diminishing photocatalytic performance.[66] A detailed optical characterization will be considered in future work to provide quantitative evidence supporting this phenomenon (Fig. 9).[65]

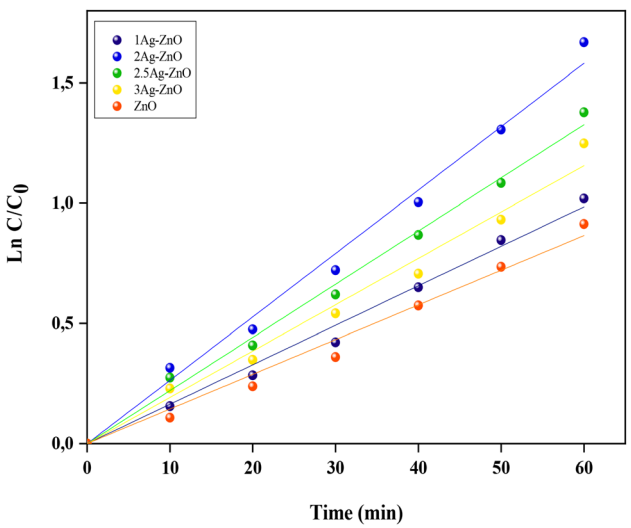


Fig. 7 CFX photodegradation first order kinetics plot (catalyst dosage 0.1 g L$^{-1}$, CFX conc. 10 mg L$^{-1}$ and free pH).

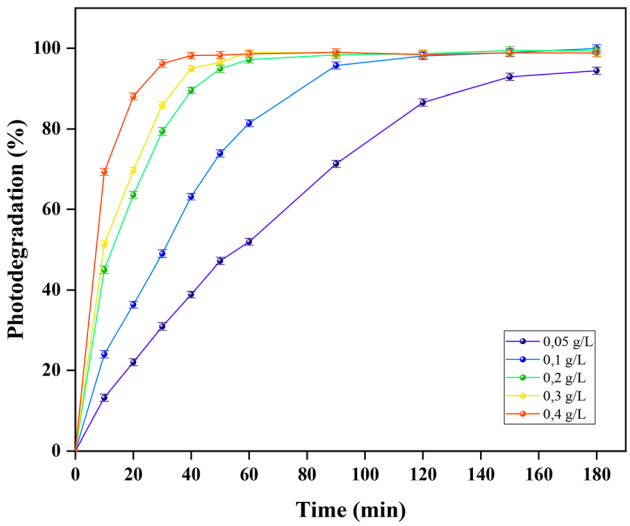


Fig. 8 Effect of catalyst amount on percentage degradation of CFX (CFX conc. 10 ppm, free pH).

**3.2.3. Effect of initial CFX concentration.** The photodegradation efficiency of CFX at various preliminary concentrations (10, 20, 30, 40, and 50 mg L$^{-1}$) was examined, as depicted in Fig. 10, under experimental conditions of a catalyst dose of 0.1 g L$^{-1}$ and free pH. The results reveal a notable behavior, when the concentration of CFX rises, the photodegradation effectiveness progressively reduces. Furthermore, at high CFX concentration a more molecules are available, the solution becomes optically denser, reducing the light penetration through the catalyst suspension. This diminished light penetration inhibits the activation of the photocatalyst, further reducing its efficiency. Moreover, the CFX molecules in solution may function as light-absorbing agents, obstructing the catalyst surface from light and hindering the photocatalytic activity. is available to generate superoxide and hydroxyl radicals (Fig. 11).[65]

**3.2.4. Effect of pH.** As indicated in previous studies,[67] the pH value is a crucial factor that greatly affects the efficiency of photodegradation processes. The current study evaluate the

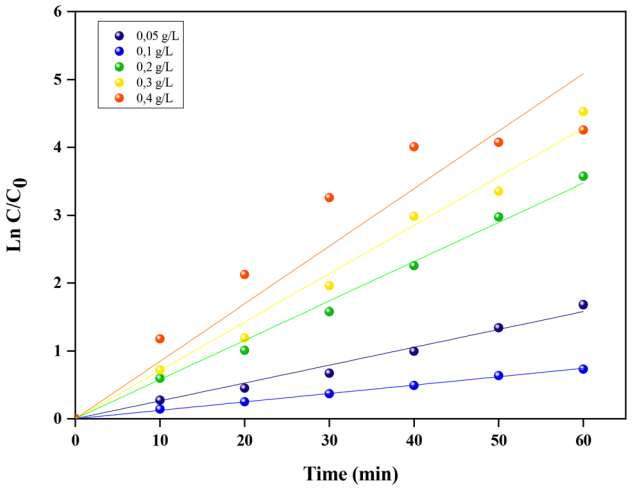


Fig. 9 CFX photodegradation first order kinetics plot (CFX conc. 10 ppm, free pH).

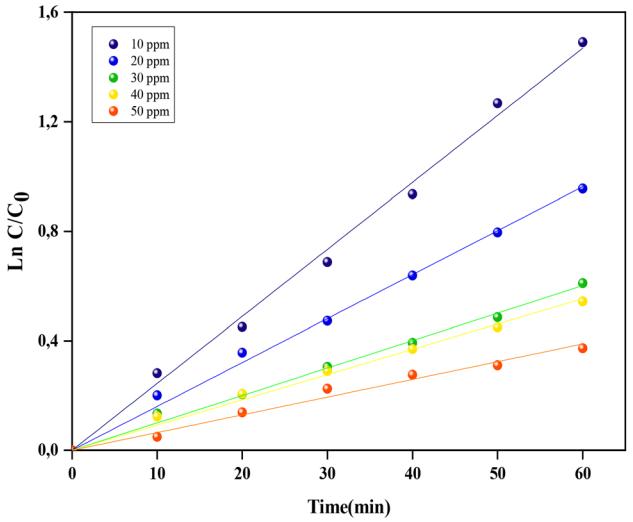


Fig. 11 CFX photodegradation first order kinetics plot (catalyst dose 0.1 g $L^{-1}$, free pH).

influence of starting pH on the photodegradation of CFX across a pH interval of 3 to 10. The tests performed utilized a catalyst quantity of 100 mg $L^{-1}$, an irradiation duration of 180 minutes, and a constant initial CFX concentration of 10 mg $L^{-1}$.

The surface charge at a specific pH, called the point zero charge (pHPZC) directly impacts the efficiency of the photocatalytic process by influencing the catalyst's capacity to attract or repel target molecules, the result of previose study revealed a pHPZC = 7.6 for Ag:ZnO (2%).[68] This finding suggests that there is a positive charge below and a negative charge above the Ag:ZnO (2%) surface at this pH.[69]

According to Fig. 12, which illustrates the influence of pH on the rate of photodegradation, the degradation rate increased as the pH rose from 3 to 6, reaching an optimal level at pH 6. However, when the pH increased further from 8 to 10, the degradation rate began to decline. This trend suggests that the photocatalytic activity of the system is highly pH-dependent, with acidic to near-neutral conditions favoring higher degradation rates, while alkaline conditions lead to a reduction in efficiency, at more acidic pH, specifically at pH = 3, the rate of CFX photodegradation decreases, and this is due to several factors. First, at this low pH, some CFX molecules can become more protonated, acquiring a positive charge. This contributes to an elctrostatic repulsion forces between the catalyst surface (positively charged at this pH) and the CFX molecules preventing the effective adsorption of pollutant molecules on the catalyst surface where hydroxyl radicals are produced.[70] An additional factor that may contribute to the photodegradation process's decreased activity is the dissolving of partial ZnO from the catalyst surface in pH 3, this degradation of the catalyst material further reduces its photocatalytic efficiency.[71]

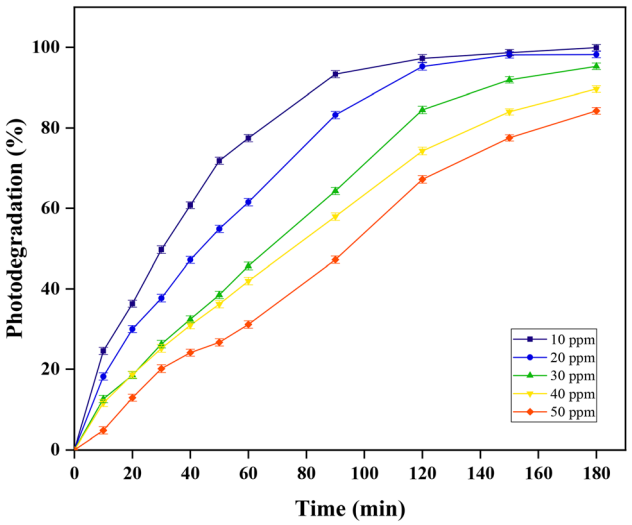


Fig. 10 Effect of initial CFX concentration on percentage degradation of CFX (catalyst dose 0.1 g $L^{-1}$, free pH).

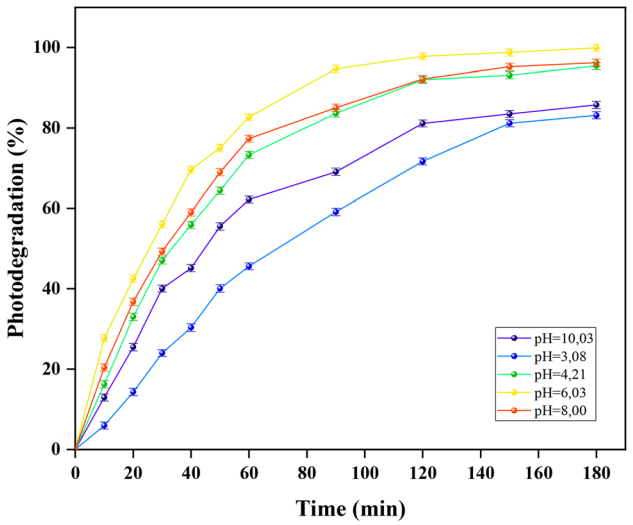


Fig. 12 Effect of pH on percentage photodegradation of CFX (catalyst dose 0.1 g $L^{-1}$ and CFX conc. 10 mg $L^{-1}$).

By increasing the pH to 6, the surface of the catalyst charge is sufficient to attract the non-bonding electrons of the nitrogen and oxygen atoms of the CFX molecules, which are not protonated at this pH with the positively charged sites on the surface of the catalyst, and consequently the rate of photodegradation increases.

As the pH is apporixmately 8, the catalyst's surface charge is almost zero charge and there is no attraction to the CFX molecules. At this neutral state, resulting in a lower degradation rate, and above this pH, the repulsion between the negatively charged surface of 2% Ag-ZnO and the unbound electron pairs of CFX's amino groups leads to a decrease in photodegradation efficiency.[70]

When the pH exceeds 8, the catalyst surface acquires a negative charge. The negatively charged surface induces electrostatic repulsion with the lone pairs of electrons on the amino groups of the CFX molecules. This repulsion further impedes adsorption by obstructing effective interaction between the CFX molecules and the catalyst's active sites. The formation and use of reactive oxygen species, such as hydroxyl and superoxide radicals, are impeded, resulting in a marked decrease in photodegradation efficiency.

### 3.3. Scavenging study

Photocatalytic degradation occurs when hydroxyl ($^{\bullet}OH$) and superoxide ($^{\bullet}O_2^-$) free radicals, with photogenerated electron–hole pairs ($e^-$, $h^+$) interact together and degrade contaminant molecules in the aqueous phase.[72] To understand the CFX photocatalytic degradation mechanism under sunlight, trapping experiments were carried out to identify the active radical species involved in order to gain a deeper understanding of the CFX photocatalytic degradation mechanism under sunlight, by introducing different scavengers including EDTA-2Na, *p*-benzoquinone (BZQ), and isopropanol (IPA) as quenchers of superoxide radical hole ($h^+$), ($^{\bullet}O_2^-$) and hydroxyl radical ($OH^{\bullet}$), respectively.[73,74] By lowering the proportion active species, these scavengers were used to stop further reactions.

As shown in Fig. 13, the introduction of scavengers such as isopropanol (IPA), *p*-benzoquinone (BZQ), and EDTA-2Na into the reaction system significantly reduces the photocatalytic degradation efficiency of CFX. Specifically, the degradation rate drops to 23.45%, 81.54%, and 91.32%, respectively, compared to the nearly complete degradation (99.87%) observed in the absence of scavengers in an aqueous medium.

This substantial reduction in degradation efficiency demonstrates the critical role of reactive species in the photocatalytic process. Among the scavengers tested, IPA, which quenches hydroxyl radicals ($^{\bullet}OH$), causes the most pronounced decline in degradation efficiency. This indicates that the main active species causing the photodegradation of cefuroxime are hydroxyl radicals.

BZQ, which targets superoxide radicals ($^{\bullet}O_2^-$), also reduces the degradation efficiency but to a lesser extent than IPA, suggesting that superoxide radicals play a supporting but less dominant role. Similarly, the effect of EDTA-2Na, a scavenger for photo-generated holes ($h^+$), indicates that these charge carriers contribute to the degradation process, albeit less significantly than hydroxyl radicals (Table 3).

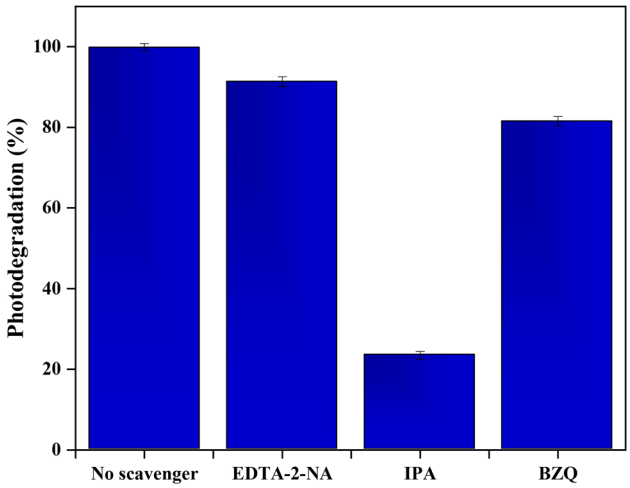


Fig. 13 Scavengers study of CFX degradation over Ag:ZnO (2%) NPs.

Table 3 Kinetic parameters related to the photocatalytic degradation of CFX for different dose of Ag:ZnO (2%)

| Catalyst dose (g $L^{-1}$) | $k$ ($min^{-1}$) | $R^2$ | $t^{1/2}$ (min) | Photodegradation (%) |
|---|---|---|---|---|
| 0.05 | 0.012 | 0.99 | 57.76 | 94.41 |
| 0.1 | 0.027 | 0.9 | 25.67 | 99.97 |
| 0.2 | 0.059 | 0.99 | 11.74 | 99.4 |
| 0.3 | 0.073 | 0.98 | 9.49 | 98.87 |
| 0.4 | 0.072 | 0.90 | 9.6 | 98.81 |

The quantitative contribution of each reactive species ($^{\bullet}OH$, $O_2^{\bullet -}$, $h^+$) was estimated using a kinetic approach. The rate constants $k$ were calculated according to the pseudo-first-order kinetic model. The following table summarizes the rate constants obtained and the relative contributions of each species.[75]

$$\text{Relative contribution } (\%) = \frac{1 - k \text{ trap}}{k \text{ without trap}} \times 100 \quad (7)$$

From these observations, it is clear that hydroxyl radicals ($^{\bullet}OH$) are the primary species driving the photocatalytic degradation of CFX (Fig. 14).

### 3.4. Mechanism of photodegradation

The photocatalytic degradation mechanism of CFX using Ag:ZnO nanoparticles under solar irradiation can be divided into two fundamental and synergistic stages: (i) adsorption of pollutant molecules and (ii) photoinduced redox reactions leading to mineralization.

In the initial step, CFX molecules diffuse toward and adsorb onto the surface of the photocatalyst. This adsorption is governed by multiple factors, including surface area, catalyst charge (dependent on pH), and functional groups present on

 

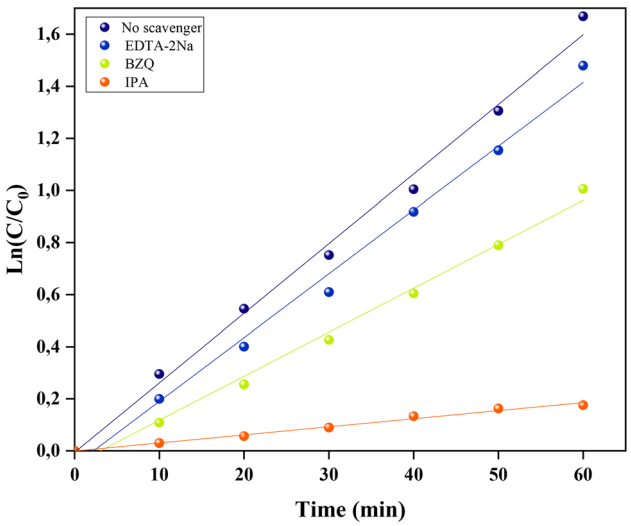


Fig. 14 CFX photodegradation first order kinetics plot by introducing different scavengers.

both the photocatalyst and the pollutant. The formation of stable surface complexes facilitates intimate contact between CFX and the photoactive sites, thereby enhancing subsequent photochemical interactions.

Upon solar light irradiation, ZnO absorbs photons with energy equal to or greater than its band gap, triggering the excitation of electrons ($e^-$) from the VB to the CB, leaving behind positively charged holes ($h^+$) in the VB:

$$ZnO + h\nu \rightarrow ZnO\ (h^+_{(VB)}) + ZnO\ (e^-_{(CB)}) \quad (8)$$

However, a critical challenge in conventional ZnO photocatalysis is the rapid recombination of these photogenerated $e^-/h^+$ pairs, which significantly reduces the formation of ROS. To circumvent this, Ag nanoparticles are introduced as electron sinks due to their lower Fermi level compared to the CB of ZnO. This energy gradient enables efficient electron transfer from ZnO to Ag, leading to spatial charge separation:

• Ag nanoparticles capture and store photogenerated electrons, while holes remain in ZnO. This not only prolongs the lifetime of charge carriers but also suppresses recombination, resulting in more active species available for redox reactions.[37]

$$Ag^+ + e^-_{(CB)} \rightarrow Ag \quad (9)$$

The electrons accumulated in Ag nanoparticles or in ZnO's CB reduce molecular oxygen dissolved in water to form superoxide radicals:

$$O_2 + e^-_{(CB)} \rightarrow O_2^{\bullet -} \quad (10)$$

These $O_2^{\bullet -}$ species can undergo further reactions with water to generate $OH^\bullet$, which are highly oxidative:

$$O_2^{\bullet -} + H_2O \rightarrow HO_2^\bullet + OH^\bullet \quad (11)$$

Simultaneously, the photogenerated holes in the VB oxidize hydroxide ions or water molecules to form additional $OH^\bullet$ radicals:

$$OH^- + h^+_{(VB)} \rightarrow OH^\bullet \quad (12)$$

$^\bullet OH$ and $^\bullet O_2^-$ are the primary oxidizing agents responsible for attacking and decomposing the CFX molecule through a series of oxidative steps, ultimately leading to its mineralization into non-toxic end-products:[68]

$$O_2^{\bullet -} + OH^\bullet + CFX = H_2O + CO_2 \quad (13)$$

The overall photodegradation thus combines photoinduced charge generation, enhanced charge separation by Ag, and formation of ROS to ensure efficient pollutant breakdown.

The scavenger experiments conducted in this study further validate the mechanistic pathway. The presence of isopropanol

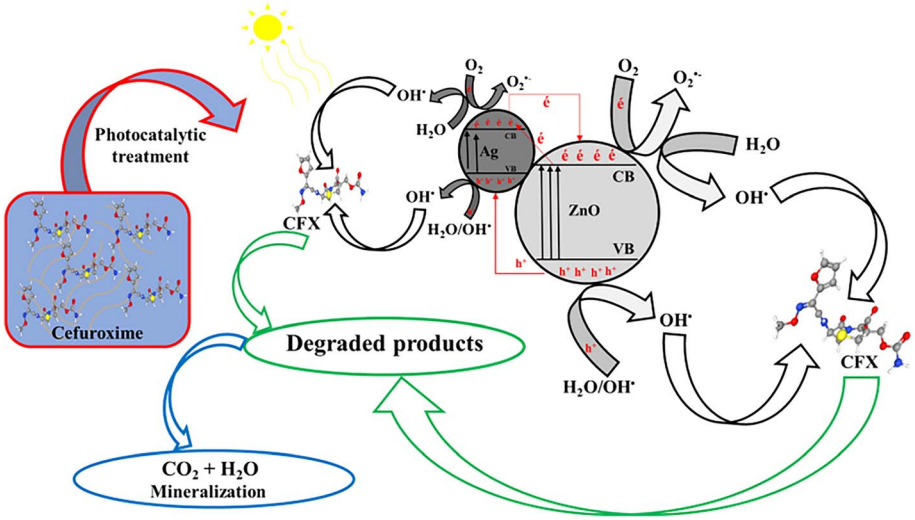


Fig. 15 Plausible photocatalytic degradation mechanism of CFX.

Table 4 Kinetic parameters related to the photocatalytic degradation of CFX (catalyst amount 0.1 g $L^{-1}$, free pH)

| CFX initial | $k$ ($min^{-1}$) | $R^2$ | $t^{1/2}$ (min) | Photodegradation (%) |
|---|---|---|---|---|
| 10 | 0.024 | 0.998 | 28.32 | 99.91 |
| 20 | 0.016 | 0.998 | 43.32 | 98.2 |
| 30 | 0.01 | 0.997 | 69.31 | 95.27 |
| 40 | 0.009 | 0.997 | 77.01 | 89.63 |
| 50 | 0.006 | 0.993 | 115.52 | 84.24 |

($^{\bullet}$OH scavenger) caused the most significant decrease in degradation efficiency, confirming that $^{\bullet}$OH is the dominant reactive species. Lesser inhibition by benzoquinone and EDTA-2Na indicates that $O_2^{\bullet-}$ and $h^+$ also contribute, albeit to a smaller extent.

The proposed photocatalytic degradation mechanism of CFX using Ag-doped ZnO nanoparticles under solar irradiation is schematically illustrated in Fig. 15. This figure visually summarizes the sequence of physicochemical processes involved, starting from the photoexcitation of ZnO and the subsequent migration of electrons to Ag nanoparticles, leading to the formation of ROS such as $^{\bullet}$OH and $^{\bullet}O_2^-$. These ROS actively participate in the oxidative degradation and mineralization of CFX into benign end-products such as $CO_2$ and $H_2O$. The figure also highlights the crucial role of Ag in enhancing charge separation and extending the catalyst's activity into the visible region, thereby improving the overall photocatalytic efficiency.

### 3.5. Mineralization of cefuroxime (CFX)

The photocatalytic efficiency of the 2% Ag-ZnO nanocomposite was assessed under solar irradiation, with emphasis on both the molecular degradation of CFX and the extent of its mineralization. The degradation process was followed by quantifying the decrease in CFX concentration over time, whereas mineralization was determined by measuring TOC removal, indicative of complete oxidation to inorganic end-products (Table 4).

The photocatalytic efficiency of the 2% Ag-ZnO nanocomposite was assessed under solar irradiation, with emphasis on both the molecular degradation of CFX and the extent of its mineralization. The degradation process was followed by quantifying the decrease in CFX concentration over time, whereas mineralization was determined by measuring TOC removal, indicative of complete oxidation to inorganic end-products (Table 5).

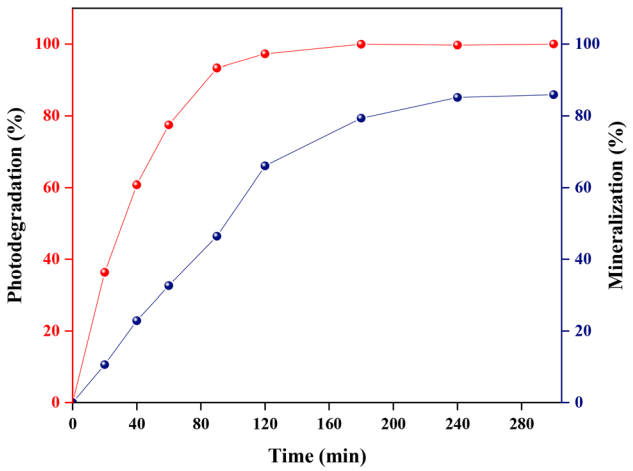


Fig. 16 CFX photodegradation and mineralization efficiencies in the presence of 2% Ag-ZnO under sunlight irradiation.

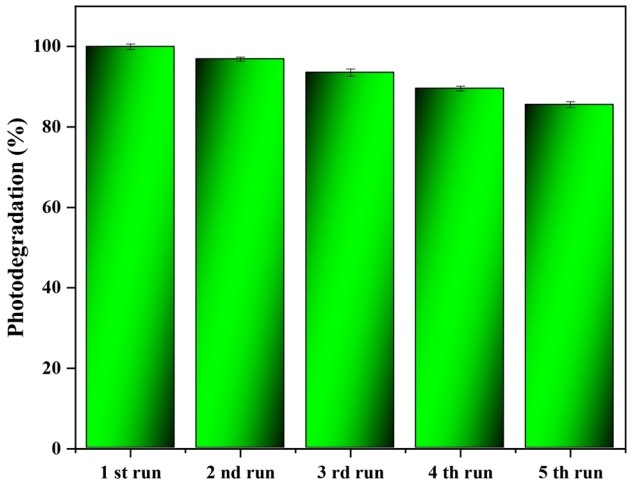


Fig. 17 Reusability of Ag:ZnO (2%) NPs toward photodegrdation of CFX.

Cefuroxime underwent rapid degradation under photocatalytic irradiation, with near elimination achieved in approximately 160 minutes. In contrast, mineralization proceeded more gradually, reaching 85.9% after 280 minutes. This difference suggests the formation of intermediate organic compounds during photocatalysis. These compounds tend to resist further oxidation by reactive oxygen species, particularly $^{\bullet}$OH, requiring prolonged irradiation time to be completely oxidized to $CO_2$ and $H_2O$.

Table 5 Scavengers used with the oxidizing species trapped, the apparent reaction rate constant ($k$) and the relative contribution

| Scavenger | Trapped species | $k$ ($min^{-1}$) | Relative contribution (%) | $R^2$ |
|---|---|---|---|---|
| No scavenger | — | 0.02673 | — | 0.99254 |
| EDTA-2Na | $h^+$ | 0.02451 | 8.3 | 0.099039 |
| BZQ | $^{\bullet}O_2^-$ | 0.01689 | 36.81 | 0.98982 |
| IPA | $^{\bullet}$OH | 0.00311 | 88.36 | 0.98648 |

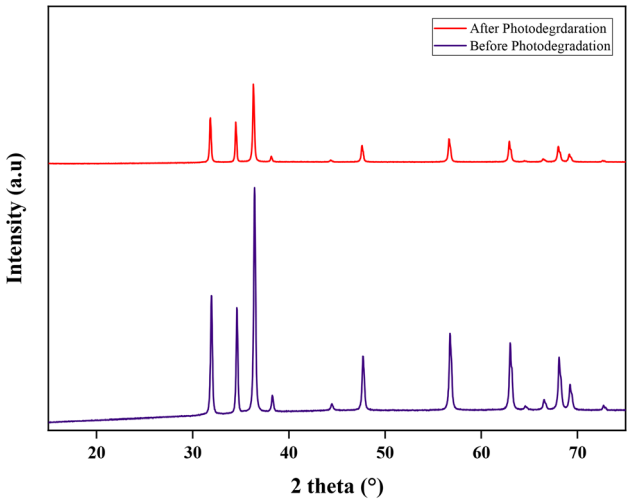


Fig. 18 XRD patterns of recycled Ag:ZnO (2%) NPs before and after photodegradation cycles.

### 3.6. Recyclability and structural retention of the 2% Ag-ZnO photocatalyst

The practical implementation of photocatalytic systems largely depends on their recyclability and stability under repeated use. To investigate the reusability potential of the synthesized 2% Ag-ZnO photocatalyst, a series of five consecutive degradation experiments of CFX were conducted under optimized solar-driven conditions, with each run lasting 180 minutes. The catalytic performance for each cycle is illustrated in Fig. 16.

After each reaction, the photocatalyst was recovered by filtration, thoroughly washed with distilled water to eliminate residual organic species, and dried at 100 °C for 8 hours prior to reuse.[44] Throughout the five cycles, the photocatalyst maintained high photocatalytic efficiency, with only a slight decrease of approximately 21% in CFX removal efficiency, highlighting its stability and suitability for repeated application (Fig. 17). This minor decline in performance could be attributed to two primary factors partial loss of photocatalyst material during the recovery steps and progressive accumulation of intermediate organic compounds that may block surface pores and active sites, consequently reducing the specific surface area and active interaction zones of the catalyst.[76] To assess possible structural alterations after repeated use, XRD analysis was performed. As depicted in Fig. 18, the XRD patterns before and after the fifth cycle show no significant variation in diffraction peak positions, confirming that the crystalline structure of the 2% Ag-ZnO catalyst remained intact after multiple photocatalytic operations.

### 3.7. Decision tree coupled with the least squares method

As mentioned earlier, hyperparameter optimization was performed to identify the best performing model to accurately predict the different output variables. This step is essential to ensure an optimal compromise between model complexity and generalization capacity. The results of this optimization, presented in Table 6, highlight the final selected hyperparameters, which led to the maximum improvement in the performance of the DT_LSBOOST model.

The optimized DT_LSBOOST model exhibits remarkable performance (Table 6), as evidenced by the extremely high $R$, close to 1 for all datasets. With values of 0.9996 for training, 0.9995 for testing, and 0.9998 for validation, the model demonstrates near-perfect correlation between predicted and experimental values. This exceptional accuracy reflects the model's ability to faithfully capture the relationship between input variables and the response under study, thus ensuring optimal prediction reliability. In addition, the RMSE remains very low, with 0.8634 for training, 0.8817 for testing, and 0.8234 for validation. These low values indicate that the differences between predicted and actual values are minimal, thus reinforcing the model's robustness. Furthermore, the small difference between training and testing performance suggests that the model is not subject to excessive overfitting, confirming its ability to generalize well to new data.

Hyperparameter optimization played a key role in the model's effectiveness. A reduced number of leaves (min leaf size: 1) and a minimum parent node size of 2 enabled detailed modeling while avoiding excessive fragmentation. A learning rate of 0.2 allowed for gradual weight updates, balancing rapid convergence and stability. Furthermore, the use of 200 maximum splits and the inclusion of surrogates to handle missing values enhanced the model's accuracy.

Table 6 Performances of the best model of DT_LSBOOST

Min leaf size: 1
Learnrate: 0.2
Surrogate: All
Min parent size: 2
Number of learng cycles: 20
Max number splits: 200

| Coefficients of correlation | | | | RMSE | | | |
|---|---|---|---|---|---|---|---|
| Train | Test | VAL | All | Train | Test | VAL | All |
| 0.9996 | 0.9995 | 0.9998 | 0.9996 | 0.8634 | 0.8817 | 0.8234 | 0.8516 |

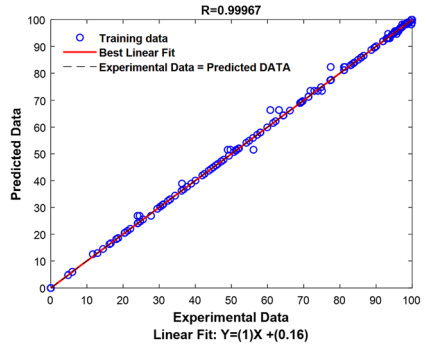


(a)

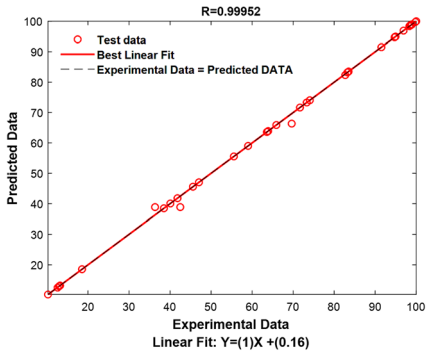


(b)

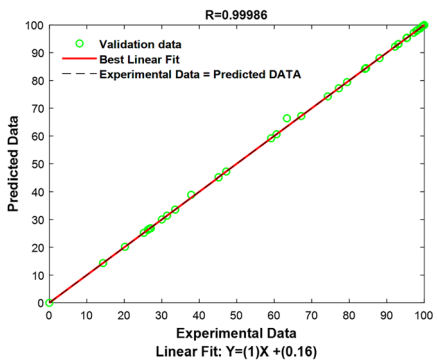


(c)

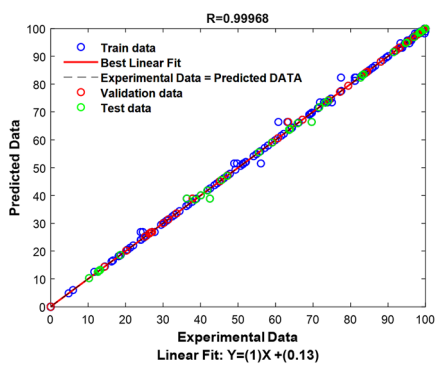


(d)

Fig. 19 Correlation between experimental results and DT_LSBOOST model predictions: (a) training set, (b) test set, (c) validation set, and (d) combined data.

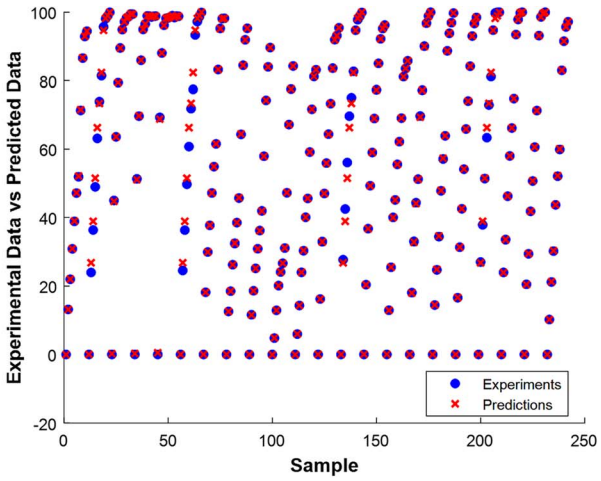


(a)

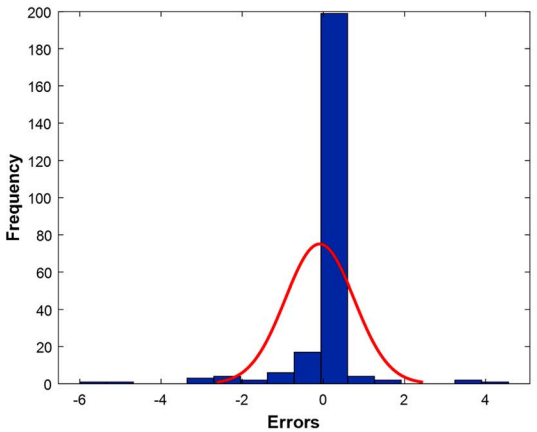


(b)

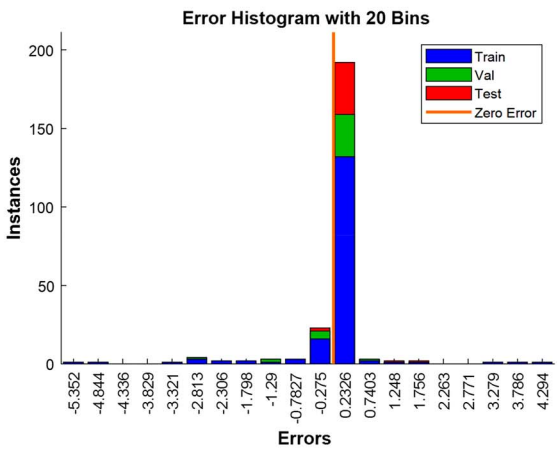


(c)

Fig. 20 Residual analysis of models developed using various techniques based on predicted values: (a) correlation between experimental and predicted sample data, (b) the error distribution and (c) error distribution across instances.

Fig. 19 visually displays the results of the DT_LSBOOST model, comparing the predicted values to the experimental values.

Overall, these results demonstrate extremely high-performance modeling, capable of providing reliable and accurate predictions. The observed stability between the training, test and validation sets demonstrates the quality of the model, which can be used with confidence for the optimization and prediction of the photodegradation rate of CFX in the presence of Ag:ZnO.

**3.7.1. Residues study.** This section provides an in-depth evaluation to measure the effectiveness of the selected model. The analysis is based on the residual method, combined with two types of histograms: one illustrating the distribution of errors across all cases studied and the other representing the error frequency during the training, testing, and validation phases.[77–80] The residual method allows a direct comparison between experimental values and model predictions by integrating all data from the different phases. This approach was implemented to detect potential systemic anomalies or inconsistencies in the model predictions.[81,82] The results, presented in Fig. 20a, confirm that the model's accuracy is consistent with the experimental data. In addition, a detailed error analysis was performed using a histogram illustrating the deviations between observed and predicted values (Fig. 20b). This representation allows for examining model variability and identifying potential error trends.[83,84] Additionally, an error frequency study was conducted for each phase (training, testing, and validation) to assess the robustness of the model. Fig. 20c illustrates this analysis, providing a detailed view of the error distribution and allowing the reliability of the model's predictions to be judged.[85,86]

Fig. 20a shows the overlay of experimental and predicted values, revealing a close correspondence between these two datasets. This correlation highlights the model's ability to provide predictions extremely close to actual values, thus attesting to its accuracy and effectiveness in modeling the analyzed phenomenon.

Fig. 20b illustrates the error distribution, indicating that approximately 200 errors out of a total of 242 observations are around zero. This concentration suggests that the majority of deviations between observed and estimated values are very small, falling within a narrow range of [−2.5; 2.5]. This distribution of errors demonstrates that the model is capable of generating highly accurate predictions, with minimal deviation from actual values. Finally, Fig. 20c confirms the model's excellent performance by showing that errors remain predominantly centered around zero throughout the training, testing, and validation phases. This consistency across all training steps indicates a high robustness of the model, which maintains a low margin of error regardless of the dataset used. These results demonstrate not only the accuracy of the model, but also its ability to generalize effectively, thus ensuring reliable and consistent predictions across all analyzed data.

**3.7.2. Optimization of optimal conditions using the dragonfly algorithm.** The DA is an optimization metaheuristic inspired by the collective behavior of dragonflies during foraging and migration. It is based on five key forces: separation, alignment, cohesion, attraction to a food source, and predator avoidance.[87] These forces enable agents to efficiently explore the search space and converge toward optimal solutions. In its exploration phase, dragonfly favors solution dispersion to avoid local minima, while in its exploitation phase, it refines solutions by promoting convergence toward the best values found.[4] Thanks to this balance between exploration and exploitation, DA is widely used to solve complex optimization problems in various fields, including engineering, artificial intelligence, and network optimization. Compared to other evolutionary algorithms, DA stands out for its simplicity of implementation, its ability to handle multidimensional search spaces, and its rapid convergence.[87] However, like any metaheuristic algorithm, its effectiveness depends on the parameter settings and the problem to be addressed.[87] To improve its performance, it is often coupled with other techniques, such as machine learning algorithms or hybrid optimization strategies.

DA was used in this study to identify optimal CFX degradation conditions based on the DT_LSBOOST model, designed and validated in this work. DA optimizes the DT_LSBOOST model parameters and determines the best input variable configurations to improve the accuracy of CFX degradation predictions. Its use also aims to optimize the model's efficiency by identifying the most favorable conditions for the degradation process, while taking into account the complexity of interactions between the various influencing factors.

Table 7 Results of optimisation optimal and validation

| DA: Agent search number: 50 Number of iterations: 100 | |
|---|---|
| Concentration of CFX: 50 mg $L^{-1}$ | |
| Optimal condition | X1 = 180, X2 = 0.100, X3 = 50, X4 = 6.11, X5 = 2 |
| Predicted CFX photodegradation rate | 85.1998% |
| Experimental CFX photodegradation rate | 84.2466% |
| Error | 0.9532% |

The results of the optimization performed using the DA algorithm, as well as the ideal conditions determined for CFX degradation, are presented in Table 7. This table lists the optimal parameter values obtained using the DT_LSBOOST model and validated experimentally. In addition, the values predicted by the model under these optimal conditions were compared with the experimental results obtained after validation, allowing for an assessment of the model's reliability in a real-world context. The deviation between predicted and experimental values was also calculated and included in Table 7, highlighting the accuracy of the model in estimating the CFX degradation rate. A low deviation between these values confirms the model's ability to provide robust and reliable predictions, thus demonstrating the effectiveness of the DT_LSBOOST approach combined with DA optimization. These results validate the application of this methodology to determine the best experimental conditions and maximize the performance of the studied process.

The optimization results obtained using DA (Table 7) were carefully analyzed to identify the optimal experimental conditions for CFX photodegradation. In this approach, the DA algorithm was applied with 50 search agents and 100 iterations, thus ensuring a thorough exploration of the parameter space. The optimization allowed the determination of precise values for the variables influencing the process: a reaction time of 180 minutes, a catalyst dosage of 0.1 g $L^{-1}$, an initial CFX concentration of 50 mg $L^{-1}$, a pH of 6.11, and a silver (Ag) doping percentage of 2%. The DT_LSBOOST model, coupled with the DA algorithm, was used to estimate the optimal CFX photodegradation rate under these conditions. The model's predictions indicate a degradation rate of 85.1998%, while the experiment revealed a very close value of 84.2466%. The difference between these two values was quantified by a relative error of 0.9532%, demonstrating the model's high accuracy in predicting the process under study. This low margin of error confirms that the DA algorithm was particularly effective in refining the experimental conditions and improving the performance of the prediction model. Indeed, optimization identifies the most influential parameters and maximizes the efficiency of the CFX degradation process. Furthermore, the consistency between the predicted and experimental values demonstrates the robustness and reliability of the DT_LSBOOST model under real-world conditions. These results validate the combined use of the DA algorithm and the DT_LSBOOST model for optimizing the CFX photodegradation process. This methodology constitutes a promising approach to precisely adjust experimental conditions, thus ensuring efficient degradation of the pollutant while minimizing the uncertainty of predictions.

**3.7.3. Interface for optimization and prediction.** An advanced application was developed in MATLAB to accurately predict the photodegradation rate of CFX based on experimental conditions, using the DT_LSBOOST model (Fig. 21). This application is based on the integration of an intelligent modeling and optimization system, combining the robustness of the DT_LSBOOST model for prediction and DA for parameter optimization.

First, the application uses the DT_LSBOOST model to estimate the photodegradation rate of CFX based on five input parameters: reaction time (X1), catalyst dose (X2), initial CFX concentration (X3), pH (X4), and Ag doping percentage (X5).

Next, an optimization module was integrated into the application to identify the ideal experimental conditions that maximize CFX photodegradation efficiency. This optimization is

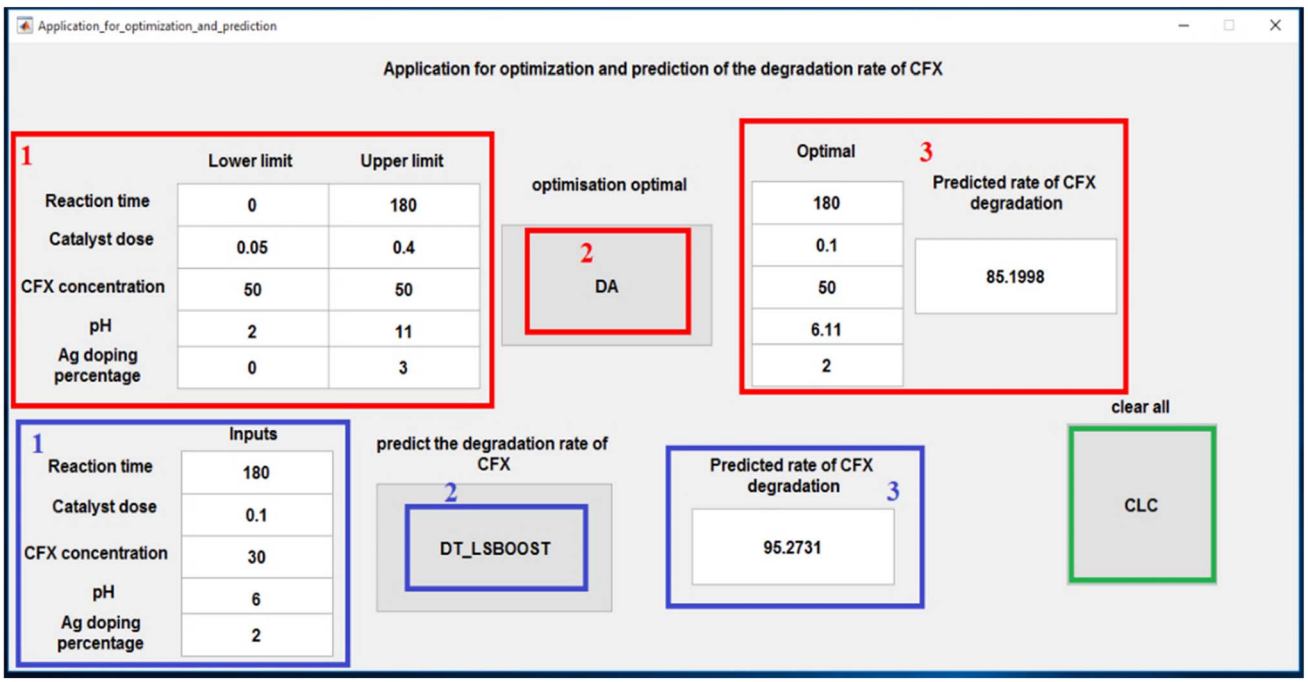


Fig. 21 MATLAB interface for predicting CFX photodegradation using DT_LSBOOST and optimization with the DA algorithm.

performed using DA, which simulates the collective behavior of dragonflies to explore the solution space and find the best experimental parameters. The algorithm iteratively adjusts the input variables to achieve an optimal degradation rate while minimizing prediction errors. The application thus offers dual functionality: (i) reliable prediction of the CFX photodegradation rate based on the chosen experimental conditions and (ii) automatic parameter optimization to maximize process efficiency. It constitutes a powerful tool for researchers and engineers working on advanced pollutant degradation, enabling a better understanding of the underlying phenomena and significantly improving the performance of the system under study. Importantly, since the DT_LSBOOST model has been rigorously trained, tested, and validated using experimental data with excellent agreement between predicted and observed degradation rates (less than 1% error), the developed application enables the replacement of further experimental trials by accurate simulation. Once the model is validated, as in our case, simulation can confidently be used to explore a wide range of operational conditions, predict degradation efficiency, and guide experimental design. This justifies the creation of the MATLAB application as a predictive and decision-support tool that significantly reduces the need for repeated laboratory experiments.

## 4. Conclusion

In this study, silver-doped zinc oxide (Ag-ZnO) nanoparticles were successfully synthesized and characterized for their enhanced photocatalytic degradation of cefuroxime (CFX) under solar irradiation. Structural analyses confirmed the effective incorporation of Ag into the ZnO matrix, leading to significant modifications in optical and electronic properties, particularly a reduced bandgap energy and improved charge carrier separation. Among the different doping ratios, 2 wt% Ag:ZnO exhibited the highest degradation efficiency, achieving 99.97% CFX removal under optimal conditions. The superior performance of Ag-ZnO was attributed to the synergistic effect of Ag doping, which minimized electron–hole recombination and extended the absorption spectrum towards the visible range. To systematically optimize the photocatalytic process, a Decision Tree coupled with the Least Squares Boosting (DT_LSBOOST) model was developed. The predictive model demonstrated outstanding accuracy ($R > 0.9996$) with a minimal root mean square error (RMSE < 0.88), underscoring its ability to reliably estimate photodegradation efficiency under various experimental conditions. Additionally, the Dragonfly Algorithm (DA) was employed for hyperparameter optimization, successfully identifying the ideal reaction conditions: pH = 6.11, catalyst dosage = 0.1 g $L^{-1}$, initial CFX concentration = 50 mg $L^{-1}$, and a reaction time of 180 minutes. Under these optimized conditions, an experimentally validated degradation rate of 84.25% was achieved, demonstrating the efficacy of AI-driven process optimization. The findings of this study highlight the potential of Ag:ZnO nanostructures as efficient photocatalysts for antibiotic removal from wastewater, while also emphasizing the crucial role of machine learning-based modeling in refining photocatalytic processes. This integration of advanced materials science with computational intelligence offers a scalable and data-driven approach for environmental remediation. Future research should focus on assessing the long-term stability of Ag-ZnO nanostructures in real wastewater matrices, evaluating their reusability, and exploring their potential in degrading a broader spectrum of pharmaceutical contaminants. Furthermore, hybrid AI-optimization frameworks could be expanded to multi-objective optimization, considering energy consumption and economic feasibility to enhance the practical applicability of photocatalytic water treatment systems.

## Conflicts of interest

The authors declare that they have no competing interests.

## Data availability

The data presented in this study 813 are available in the manuscript. See DOI: https://doi.org/10.1039/d5ra04447b.

## Funding

This work was supported and funded by the Deanship of Scientific Research at Imam Mohammad Ibn Saud Islamic University (IMSIU) (grant number IMSIU-DDRSP2502).

## References

1 W. Stambouli, N. Nasrallah, D. Fedoul and A. A. Assadi, *Journal of Water Process Engineering*, 2025, **76**, 108213.
2 M. Kebir, R. Bouallouche, N. Nasrallah, H. Tahraoui, N. Elboughdiri, F. Ait Merzeg, F. Dergal, S. Amirouche, A. A. Assadi and A. Amrane, *Catalysts*, 2024, **14**, 875.
3 X. Duan, Y. Huang, C. Shen, P. Jones and X. Deng, *Indoor Air*, 2025, **2025**, 1071778.
4 H. Tahraoui, A.-E. Belhadj, Z. Triki, N. R. Boudellal, S. Seder, A. Amrane, J. Zhang, N. Moula, A. Tifoura and R. Ferhat, *Process Saf. Environ. Prot.*, 2023, **169**, 909–927.
5 E. E. Hernández-Coronado, E. J. Ruiz-Ruiz, L. Hinojosa-Reyes, F. J. Beltrán, J. López-Gallego, M. Gracia-Pinilla and M. Villanueva-Rodríguez, *J. Environ. Chem. Eng.*, 2021, **9**, 1–11.
6 H. Tahraoui, A.-E. Belhadj, A. Amrane, S. Toumi, B. Jaouadi and J. Zhang, *J. Taiwan Inst. Chem. Eng.*, 2024, **165**, 105783.
7 Y. Pan, H. Liu, Z. Huang, W. Zhang, H. Gao, L. Liang, L. Dong and H. Meng, *Angew. Chem.*, 2024, **136**, e202316315.
8 J. Rossmann, S. Schubert, R. Gurke, R. Oertel and W. Kirch, *J. Chromatogr. B: Anal. Technol. Biomed. Life Sci.*, 2014, **969**, 162–170.
9 H. Du, A. Zhang, Q. Zhang, Y. Sun, H. Zhu, H. Wang, Z. Tan, X. Zhang and G. Chen, *Sep. Purif. Technol.*, 2025, **359**, 130597.
10 A. Husain Khan, H. Abdul Aziz, P. Palaniandy, M. Naushad, E. Cevik and S. Zahmatkesh, *Chemosphere*, 2023, **339**, 139647.

11 A. Abdykadyrov, S. Marxuly, Y. Tashtay, A. Kuttybayeva, G. Sharipova, K. Anar and P. Akylzhan, *Water Conserv. Manag.*, 2023, **7**, 148–157.
12 Q. Yang, Y. Gao, J. Ke, P. L. Show, Y. Ge, Y. Liu, R. Guo and J. Chen, *Bioengineered*, 2021, **12**, 7376–7416.
13 M. Aminul Islam, M. K. Nazal, M. Sajid and M. Altahir Suliman, *J. Mol. Liq.*, 2024, **396**, 123976.
14 M. I. Kanjal, M. Muneer, M. A. Jamal, T. H. Bokhari, A. Wahid, S. Ullah, A. Amrane, A. Hadadi, H. Tahraoui and L. Mouni, *Sustainability*, 2023, **15**, 7256.
15 M. Smara, R. Khalladi, N. Moulai-Mostefa, K. Madi, D. Mansour, S. Lekmine, O. Benslama, H. Tahraoui, J. Zhang and A. Amrane, *Processes*, 2024, **12**, 621.
16 D. Mansour, E. Alblawi, A. K. D. Alsukaibi, J. Humaidi, H. Tahraoui, M. Shatat, S. Teka, S. Maisara, N. Bellakhal and H. Binous, *Water*, 2024, **16**, 1964.
17 M. Kebir, I.-K. Benramdhan, N. Nasrallah, H. Tahraoui, N. Bait, H. Benaissa, R. Ameraoui, J. Zhang, A. A. Assadi and L. Mouni, *Catal. Commun.*, 2023, **183**, 106780.
18 J. Wang and R. Zhuan, *Sci. Total Environ.*, 2020, **701**, 135023.
19 N. Mihoubi, S. Ferhat, M. Nedjhioui, B. Zenati, S. Lekmine, R. Boudraa, M. S. Ola, J. Zhang, A. Amrane and H. Tahraoui, *Water*, 2025, **17**, 888.
20 H. Chen, C. Ng, N. H. Tran, L. Haller, S. G. Goh, F. R. Charles, Z. Wu, J. X. Lim and K. Y. H. Gin, *Sci. Total Environ.*, 2024, **924**, 171723.
21 K. O. Imwene, E. Ngumba and P. K. Kairigo, *J. Environ. Manage.*, 2022, **322**, 116065.
22 K. Madi, D. Chebli, H. Ait Youcef, H. Tahraoui, A. Bouguettoucha, M. Kebir, J. Zhang and A. Amrane, *Catalysts*, 2024, **14**, 62.
23 S. Touahri, O. Halimi, M. Zaabat, S. Mammeri, B. Boudine, M. Sebais, H. Tahraoui, J. Zhang and A. Amrane, *J. Phys. Chem. Solids*, 2024, 112299.
24 O. Baaloudj, H. Kenfoud, A. K. Badawi, A. A. Assadi, A. El Jery, A. A. Assadi and A. Amrane, *Catalysts*, 2022, **12**, 500.
25 A. N. E. H. Sid, H. Tahraoui, M. Kebir, M. A. Bezzekhami, B. Kouini, A. H. Hassein-Bey, T. Selma, A. Amrane, A. Imessaoudene and L. Mouni, *Sustainability*, 2023, **15**, 3375.
26 H. Tahraoui, A.-E. Belhadj, N. Moula, S. Bouranene and A. Amrane, *Kem. U Ind.*, 2021, **70**, 675–691.
27 N. Li, G. P. Sheng, Y. Z. Lu, R. J. Zeng and H. Q. Yu, *Water Res.*, 2017, **111**, 204–212.
28 Q. Fang, Q. Sun, R. Zhong, H. Wang and J. Qi, *Mater. Today Chem.*, 2025, **46**, 102770.
29 X. Yang, Z. Chen, W. Zhao, C. Liu, X. Qian, M. Zhang, G. Wei, E. Khan, Y. Hau Ng and Y. Sik Ok, *Chem. Eng. J.*, 2021, **405**, 126806.
30 M. Abdelkader, A. A. Assadi, M. Guiza, W. Elfalleh, L. Khezami, H. Tahraoui, O. Baaloudj, L. Mouni, J. Zhang and A. Amrane, *Catalysts*, 2025, **15**, 262.
31 S. Redjili, H. Ghodbane, H. Tahraoui, L. Abdelouahed, D. Chebli, M. S. Ola, A. A. Assadi, M. Kebir, J. Zhang and A. Amrane, *Catalysts*, 2025, **15**, 256.
32 K. Madi, F. Agueniou, D. Chebli, H. Tahraoui, A. Bouguettoucha, J. Zhang and A. Amrane, *Colloids Surf., A*, 2025, 136469.
33 J. Fang, X. Xu, Y. Yang, Z. Han, Z. Zuo, W. Han and B. Lin, *J. Therm. Anal. Calorim.*, 2025, **150**, 7335–7347.
34 O. Baaloudj, N. N. Vu, A. A. Assadi, V. Q. Le and P. Nguyen-Tri, *Adv. Colloid Interface Sci.*, 2024, **327**, 103136.
35 A. Krishnan, A. Swarnalal, D. Das, M. Krishnan, V. S. Saji and S. M. A. Shibli, *J. Environ. Sci. China*, 2024, **139**, 389–417.
36 S. Roguai and A. Djelloul, *Inorg. Chem. Commun.*, 2023, **157**, 111372.
37 M. Samadi, M. Zirak, A. Naseri, E. Khorashadizade and A. Z. Moshfegh, *Thin Solid Films*, 2016, **605**, 2–19.
38 M. A. Hajjaji, K. Missaoui, K. Trabelsi, A. Bouzaza, A. Hajjaji, B. Bessais and A. A. Assadi, *J. Photochem. Photobiol., A*, 2025, **458**, 115975.
39 F. Achouri, S. Corbel, L. Balan, K. Mozet, E. Girot, G. Medjahdi, M. Ben Said, A. Ghrabi and R. Schneider, *Mater. Des.*, 2016, **101**, 309–316.
40 P. Pascariu, C. Cojocaru, V. Ciornea, C. Romanitan and A. B. Serban, *Mater. Today Sustain.*, 2024, **26**, 100719.
41 A. Esbergenova, M. Hojamberdiev, Z. C. Kadirova, Y. Sugai, S. Mamatkulov, R. Jalolov, D. Kong, X. Qin, S. S. Daminova, O. Ruzimuradov and U. Shaislamov, *Curr. Appl. Phys.*, 2024, **67**, 18–29.
42 A. Samanta, M. N. Goswami and P. K. Mahapatra, *Phys. E*, 2024, **158**, 115885.
43 C. Chen, P. Lei, H. Ji, W. Ma, J. Zhao, H. Hidaka and N. Serpone, *Environ. Sci. Technol.*, 2004, **38**, 329–337.
44 H. Hafsa, N. Nasrallah, S. Zeghbib, M. Kebir, H. Tahraoui, A. A. Assadi, L. Khezami, A. Alghamdi, N. Dahdouh, S. Lekmine and A. Amrane, *Arab. J. Sci. Eng.*, 2025, DOI: 10.1007/s13369-025-10394-5.
45 S. Kaur and B. Pal, *J. Water Process Eng.*, 2024, **58**, 104765.
46 Md. A. I. Molla, M. Furukawa, I. Tateishi, H. Katsumata and S. Kaneco, *J. Environ. Sci. Health, Part A*, 2019, **54**, 914–923.
47 H. Tahraoui, S. Toumi, A. H. Hassein-Bey, A. Bousselma, A. N. E. H. Sid, A.-E. Belhadj, Z. Triki, M. Kebir, A. Amrane and J. Zhang, *Water*, 2023, **15**, 2631.
48 H. Tahraoui, A. Amrane, A.-E. Belhadj and J. Zhang, *Environ. Technol. Innov.*, 2022, **27**, 102419.
49 S. Mechati, M. Zamouche, H. Tahraoui, O. Filali, S. Mazouz, I. N. E. Bouledjemer, S. Toumi, Z. Triki, A. Amrane and M. Kebir, *Water*, 2023, **15**, 4274.
50 M. Nedjhioui, N. Nasrallah, M. Kebir, H. Tahraoui, R. Bouallouche, A. A. Assadi, A. Amrane, B. Jaouadi, J. Zhang and L. Mouni, *Processes*, 2023, **11**, 1314.
51 M. Zamouche, H. Tahraoui, S. Lemouedda, I. Madoui, S. Mechati, Z. Laggoun, Z. Triki, M. Kebir, J. Zhang, A. Amrane and L. Mouni, *Euro-Mediterr. J. Environ. Integr.*, 2025, DOI: 10.1007/s41207-024-00630-z.
52 H. Chelghoum, N. Nasrallah, H. Tahraoui, M. F. Seleiman, M. M. Bouhenna, H. Belmeskine, M. Zamouche, S. Djema, J. Zhang and A. Mendil, *Catalysts*, 2024, **14**, 831.
53 H. Moussa, F. Dahmoune, S. Lekmine, A. Mameri, H. Tahraoui, S. Hamid, N. Benzitoune, N. Moula, J. Zhang and A. Amrane, *Process Biochem.*, 2024, **147**, 476–488.

54 A. Guediri, A. Bouguettoucha, H. Tahraoui, D. Chebli, J. Zhang, A. Amrane, L. Khezami and A. A. Assadi, *Water*, 2024, **16**, 1208.
55 A. Guediri, A. Bouguettoucha, H. Tahraoui, D. Chebli, A. Amrane and J. Zhang, *J. Mol. Liq.*, 2024, 124860.
56 S. Toumi, S. Lekmine, N. Touzout, H. Moussa, N. Elboughdiri, R. Boudraa, O. Benslama, M. Kebir, S. Danish and J. Zhang, *Water*, 2024, **16**, 3380.
57 H. Tahraoui, S. Toumi, A. H. Hassein-Bey, A. Bousselma, A. N. E. H. Sid, A.-E. Belhadj, Z. Triki, M. Kebir, A. Amrane and J. Zhang, *Water*, 2023, **15**, 2631.
58 N. S. Mohan, A. Arulraj, R. V. Mangalaraja, R. Anitha and V. Vijayalakshmi, *Desalin. Water Treat.*, 2024, **320**, 100802.
59 R. Kumar, D. Rana, A. Umar, P. Sharma, S. Chauhan and M. S. Chauhan, *Talanta*, 2015, **137**, 204–213.
60 V. Vaiano, M. Matarangolo, J. J. Murcia, H. Rojas, J. A. Navío and M. C. Hidalgo, *Appl. Catal., B*, 2018, **225**, 197–206.
61 T. Chitradevi, A. Jestin Lenus and N. Victor Jaya, *Mater. Res. Express*, 2019, **7**, 1–11.
62 L. Zhang, X. F. Cao, X. T. Chen and Z. L. Xue, *J. Colloid Interface Sci.*, 2011, **354**, 630–636.
63 S. M. H. AL-Jawad, S. H. Sabeeh, A. A. Taha and H. A. Jassim, *J. Sol-Gel Sci. Technol.*, 2018, **87**, 362–371.
64 M. Shakir, M. Faraz, M. A. Sherwani and S. I. Al-Resayes, *J. Lumin.*, 2016, **176**, 159–167.
65 S. Mohammadzadeh, M. E. Olya, A. M. Arabi, A. Shariati and M. R. Khosravi Nikou, *J. Environ. Sci. China*, 2015, **35**, 194–207.
66 D. Curcó, J. Giménez, A. Addardak, S. Cervera-March and S. Esplugas, *Catal. Today*, 2002, **76**, 177–188.
67 A. M. Oda, H. Khuder, R. Hashim, A. Rasheed, A. A. Hasan, H. Hazim and Z. Raheem, *Res. J. Pharm. Biol. Chem. Sci.*, 2016, **7**, 2915–2924.
68 A. A. El-Bindary, A. Ismail and E. F. Eladl, *J. Mater. Environ. Sci.*, 2019, **10**, 1258–1271.
69 K. Ravichandran, N. Siva Jyothi, K. Thirumurugan, S. Suvathi, N. Chidhambaram, R. Uma and B. Sundaresan, *Chem. Phys.*, 2023, **564**, 111714.
70 A. Nezamzadeh-Ejhieh and Z. Salimi, *Desalination*, 2011, **280**, 281–287.
71 I. A. Mudunkotuwa, T. Rupasinghe, C. M. Wu and V. H. Grassian, *Langmuir*, 2012, **28**, 396–403.
72 D. Chatterjee and S. Dasgupta, *J. Photochem. Photobiol., C*, 2005, **6**, 186–205.
73 S. N. Nguyen, T. K. Truong, S. J. You, Y. F. Wang, T. M. Cao and V. Van Pham, *ACS Omega*, 2019, **4**, 12853–12859.
74 M. Ahmad, I. Ahmad, E. Ahmed, M. S. Akhtar and N. R. Khalid, *J. Mol. Liq.*, 2020, **311**, 113326.
75 J. T. Schneider, D. S. Firak, R. R. Ribeiro and P. Peralta-Zamora, *Phys. Chem. Chem. Phys.*, 2020, **22**, 15723–15733.
76 A. Payan, M. Fattahi, S. Jorfi, B. Roozbehani and S. Payan, *Appl. Surf. Sci.*, 2018, **434**, 336–350.
77 M. Kebir, H. Tahraoui, M. Chabani, N. Noureddine, A. A. Assadi, A. Amrane, N. Ben Hamadi, L. Khezami, M. Trari, N. Noureddine, A. A. Assadi, A. Amrane, N. Ben Hamadi and L. Khezami, *Processes*, 2023, **11**, 363.
78 S. Mechati, M. Zamouche, H. Tahraoui, O. Filali, S. Mazouz, I. N. E. Bouledjemer, S. Toumi, Z. Triki, A. Amrane and M. Kebir, *Water*, 2023, **15**, 4274.
79 M. Kebir, H. Tahraoui, I. K. Benramdane, N. Nasrallah, S. Toumi, J. Zhang and A. Amrane, *Water Resour. Ind.*, 2024, 100269.
80 M. Zamouche, H. Tahraoui, Z. Laggoun, S. Mechati, R. Chemchmi, M. I. Kanjal, A. Amrane, A. Hadadi and L. Mouni, *Processes*, 2023, **11**, 364.
81 H. Tahraoui, A.-E. Belhadj, A.-E. Hamitouche, M. Bouhedda and A. Amrane, *Desalin. Water Treat.*, 2021, **217**, 181–194.
82 H. Tahraoui, A.-E. Belhadj and A.-E. Hamitouche, *Kem. Ind.*, 2020, **69**, 595–602.
83 M. Zamouche, M. Chermat, Z. Kermiche, H. Tahraoui, M. Kebir, J.-C. Bollinger, A. Amrane and L. Mouni, *Water*, 2023, **15**, 493.
84 O. R. Benkouachi, A. Bouguettoucha, H. Tahraoui, A. Guediri, D. Chebli, M. Kebir, S. Knani, J. Zhang and A. Amrane, *J. Mol. Liq.*, 2024, 125951.
85 A. Hadadi, A. Imessaoudene, J.-C. Bollinger, A. Bouzaza, A. Amrane, H. Tahraoui and L. Mouni, *J. Environ. Manage.*, 2023, **331**, 117286.
86 N. Bouchelkia, H. Tahraoui, K. Benazouz, A. Mameri, R. Boudraa, H. Moussa, N. Hamri, R. Merdoud, H. Belkacemi and A. Zoukel, *Chemom. Intell. Lab. Syst.*, 2025, 105377.
87 N. Bouchelkia, H. Tahraoui, A. Amrane, H. Belkacemi, J.-C. Bollinger, A. Bouzaza, A. Zoukel, J. Zhang and L. Mouni, *Process Saf. Environ. Prot.*, 2023, **170**, 513–535.